Multi-stage Stern–Gerlach experiment modeled (with additional appendices)

Lihong V. Wang*

Department of Electrical Engineering
Andrew and Peggy Cherng Department of Medical Engineering
California Institute of Technology
1200 E. California Blvd., MC 138-78, Pasadena, CA 91125, USA

* Correspondence to LVW@caltech.edu

ORCID: 0000-0001-9783-4383

Abstract

In the classic multi-stage Stern–Gerlach experiment conducted by Frisch and Segrè, the Majorana (Landau–Zener) and Rabi formulae diverge afar from the experimental observation while the physical mechanism for electron-spin collapse remains unidentified. Here, introducing the physical co-quantum concept provides a plausible physical mechanism and predicts the experimental observation in absolute units without fitting (i.e., no parameters adjusted) with a *p*-value less than one per million, which is the probability that the co-quantum theory happens to match the experimental observation purely by chance. Further, the co-quantum concept is corroborated by statistically reproducing exactly the wave function, density operator, and uncertainty relation for electron spin in Stern–Gerlach experiments.

Keywords

Stern–Gerlach experiment; electron spin; Majorana formula; Landau–Zener formula; co-quantum dynamics; nonadiabatic transition; entanglement

1. Introduction

Performed three years before the successful development of quantum mechanics, the 1922 Stern–Gerlach experiment on silver atoms [1] quickly proved fundamental to quantum physics [2, 3]. The benchmark experiment led to the quantization of all angular momenta, discovery of electron spin, study of the measurement problem and superposition, direct investigation of the ground-state properties of atoms without electronic excitation, and selection of fully spin-polarized atoms [2]. Within a few weeks, Einstein and Ehrenfest concluded that spin collapse cannot be interpreted by radiation, which would take 100 years [4]. Recently, Wennerström and Westlund numerically simulated that relaxation of 1 μs qualitatively reproduced the double branched collapse pattern [5], and Norsen interpreted spin collapse using the de Broglie–Bohm pilot-wave theory [6]. The significance of the Stern–Gerlach experiment and relevant works are detailed in a 2016 inspiring review [2], concluding that "The physical mechanism responsible for the alignment of the silver atoms remained and remains a mystery" and quoting Feynman, "… instead of trying to give you a theoretical explanation, we will just say that you are stuck with the result of this experiment … " [7].

Immediately, Heisenberg and Einstein proposed multi-stage Stern–Gerlach experiments to explore deeper mysteries of directional quantization [2]. Ten years later, Phipps and Stern reported the first effort [8], which was unfortunately discontinued owing to Phipps' involuntary return to the US [2]. A year later, Frisch and Segrè modified the same apparatus by adopting Einstein's suggestion on the use of a single wire instead of three electromagnets to rotate spin; they also improved magnetic shielding, slit filtering, and signal detection [2]. Despite the use of three layers of magnetic shielding for the middle stage (i.e., the inner rotation chamber), the remnant or residual fringe magnetic field was still 0.42×10^{-4} T (or 0.42 G). Rather than fight the fringe magnetic field further, they took advantage of it. The magnetic field from the wire in the middle stage cancels the remnant field to produce a magnetic null point, around which the field is approximated as a magnetic quadrupole; consequently, they successfully observed nonadiabatic spin flip [9]. Note that only the magnetic field near a null point is effective for nonadiabatic spin flip; thus, the field far from a null point does not significantly affect transition, and its detailed distribution is of little import. Frisch and Segrè varied the wire current, which is the only independent variable controlled here, over nearly two orders of magnitude approximately uniformly on a logarithmic scale to observe the peak fraction of spin flip and its entire range. They started and ended with sufficiently extreme currents that yielded negligible fractions of spin flip. Having reached a nearly zero fraction of spin flip at the highest current might be the reason that they ceased increasing the current further. Further, the calculation of the fraction automatically obviates the requirement for absolute calibration. This data set suggests they designed and executed the experiment with great care.

Frisch and Segrè found that their observation [9] unexpectedly diverges from the Majorana formula (Fig. 1) [10, 11], which was stimulated by the experiment of Frisch and Segrè. The Majorana formula is a variant of the Landau–Zener formula, which is better-known despite the concurrent publications of all four related papers in the same year [12-14]. For a historical comparison of the four papers, please refer to Ref. [15]. Fermi suggested that interaction among atoms could be responsible for the divergence, but atoms were sufficiently sparse to be treated independently [9]. Rabi acknowledged "Professor E. Segrè for discussions on the details of the Frisch and Segrè experiment", recognized the role of the nuclear magnetic moment, and revised the Majorana formula through hyperfine coupling [16]. Rabi's revised formula, however, did not overcome the divergence (Fig. 1).

Multi-stage Stern–Gerlach (Frisch–Segrè) experiments are much more difficult to model than single-stage ones. Multiple stages produce far more nuanced observation because the middle stage can vary the electron spin orientation over a wide range after polarization by the first stage. A correct single-stage theory must pass the more stringent test of the multi-stage experiment. This spin-flip divergence in multi-stage Stern–Gerlach experiments remains unresolved [2]. One may only speculate why the 1933 discrepancy [9] has not been resolved. The seminal paper has not been republished in English, which might have limited its visibility.

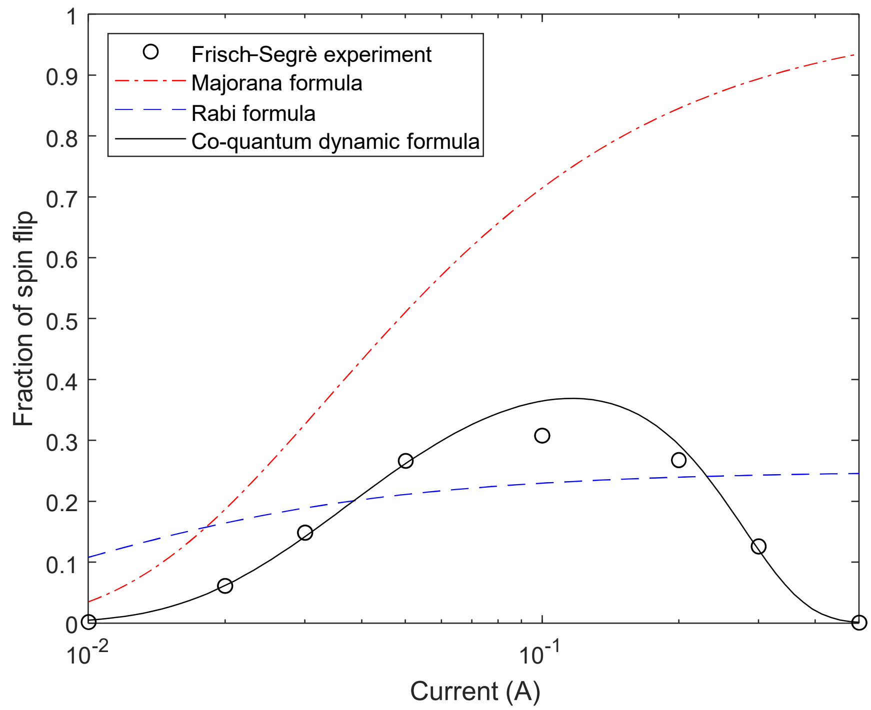

Fig. 1. Illustration of the divergence of the Majorana and Rabi formulae from the Frisch–Segrè experimental observation and the convergence of the co-quantum dynamic formula. Details are to be discussed.

Here, a theory, called co-quantum dynamics (CQD) [17], is presented to both provide a collapse mechanism and predict the Frisch–Segrè experimental observation (Fig. 1) [9]. CQD is theoretically verified by reproducing, for electron spin in Stern–Gerlach experiments, the quantum mechanical wave function, density operator, and uncertainty relation as well as, in a recent publication [17], the Schrödinger—Pauli equation. In Methods, CQD is presented in three subsections, including the equations of motion, branching condition, and pre-collapse state function and prediction expression. In Results, Stern–Gerlach experiments in both single and multiple stages are modeled. For flow continuity, lengthy interpretations are postponed to Discussion, and detailed mathematical derivations are presented in Appendices (Supplement Material). Deferred to the last appendices are the CQD derivations of the uncertainty relation, the entangled wave function, and the observation in a two-stage Stern–Gerlach apparatus with a varying angle between the quantization axes.

The following table (Table 1) compares briefly CQD with the representative existing quantum mechanical theories for collapse [18], e.g., the Ghirardi–Rimini–Weber model [19] and continuous spontaneous localization model [20, 21]. CQD, based on the classical Bloch equation (or its Landau–Lifshitz–Gilbert derivative) and the two postulates, provides a physical instead of phenomenological mechanism for electron spin collapse. In the presence of an external magnetic field, the nuclear magnetic moment is responsible for the collapse of electron spin. The absence of fitting with any adjustable parameters and the high coefficient of determination R^2 (or high correlation coefficient) led to the small p-value ($p < 8 \times 10^{-7}$) [22, 23]. In general, fitting with more and more adjustable parameters, one may improve R^2 towards unity. While R^2 is not penalized for the number of adjustable parameters used relative to the number of experimental data points available, the p-value is. Therefore, one may achieve an arbitrarily high R^2 at the expense of the p-value. The p-value is an objective measure of agreement between a theory and the experiment. As a standard definition, the p-value quantifies the probability of observing results at least as extreme as the ones observed given that the null hypothesis is true. For stringent discoveries, high-energy physics, for example, requires $p \leqslant 3 \times 10^{-7}$, which corresponds to 5σ [24]. The LIGO observation of gravitational waves applied a similar criterion [25]. The agreement of CQD with the experiment is at a similar level as well. While the LIGO observed a chirp signal, which is common in various forms in nature, the Frisch–Segrè experimental data follow an uncommon shape, which is even more unlikely to be matched by random chance. Therefore, the value of $p < 8 \times 10^{-7}$ claims a statistical significance that cannot be ignored objectively. The probability that CQD happens to match the experimental observation so well purely by chance is less than one in a million. It is even less likely for an incorrect theory to match an incorrect experiment by chance if one doubts the Frisch–Segrè experimental data. Because the Majorana or Rabi formula, if correct, follows a monotonic trend, it would be difficult to fathom that some experimental imperfections caused the fraction of spin flip to increase at low currents and to decrease at high currents. Matching a theory with the experiment so well without using any adjustable parameters inspires conviction. Further, CQD is corroborated by statistically reproducing exactly the wave function, density operator, and uncertainty relation for electron spin. This corroboration may be considered supporting evidence because an incorrect theory would highly unlikely be able to reproduce so many fundamental aspects of quantum mechanics.

Table 1. Comparison between representative existing quantum mechanical theories and CQD.

	Existing theories	**Co-quantum dynamics**
Domain	Quantum mechanical	Semiclassical
Starting equation	Schrödinger equation	Bloch equation (classical) [17]
Cause for collapse	Phenomenological: no physical object identified [18]	Physical: nuclear magnetic moment identified
Angular distribution of nuclear magnetic moment	Discrete (quantized); isotropic	Continuous; isotropic or anisotropic
Collapse rate	Preset as a constant dimensional rate (1/s)	Scaled dynamically via a dimensionless constant (Eq. 9)
Measurement uncertainty	Inequality	Equality (Eq. 186), yielding the inequality (Eq. 187)
Quantitative prediction of multi-stage Stern–Gerlach (Frisch–Segrè) experiment	Not found yet in the literature except the Majorana or Rabi formulae	Accurately ($p < 8 \times 10^{-7}$) without scaling or fitting, no parameters are adjusted

2. Methods

CQD equations of motion

In classical electrodynamics, the motion of a magnetic dipole moment, $\vec{\mu}$, is described by the Bloch equation,

$$\frac{d\hat{\mu}}{dt} = \gamma\hat{\mu} \times \vec{B}, \tag{1}$$

where caret denotes a unit vector, t time, γ the gyromagnetic ratio, and $\vec{B}$ the magnetic flux density. Majorana stated that both the classical and the quantum-mechanical treatments on spin flip require integration of the same differential equations [10, 11]. It is known that the Schrödinger or von Neumann equation for a unitary two-level system can be converted to the Bloch equation or its analog [7, 26, 27].

We now extend the Bloch equation to the Landau–Lifshitz–Gilbert equation [28],

$$\frac{d\hat{\mu}}{dt} = \gamma\hat{\mu} \times \vec{B} - k_i\hat{\mu} \times \frac{d\hat{\mu}}{dt}, \tag{2}$$

where the dimensionless k_i is called the induction factor here. Although this equation was originally intended for condensed matter, the underlying physical mechanism for the added term is compatible with CQD (see Paragraph 1 in Discussion). In fact, the author had developed CQD before realizing its connection with the Landau–Lifshitz–Gilbert equation. If $k_i = 0$, the Bloch equation is recovered.

Henceforth, subscripted e and n denote electron and nucleus, respectively. The default atom, to match the Frisch–Segrè experiment [9], is potassium (^{39}K). The scope of the manuscript is limited to potassium in the Stern–Gerlach or Frisch–Segrè experiment.

The torque-averaged magnetic flux densities from $\vec{\mu}_n$ and $\vec{\mu}_e$ applied on each other are respectively (Appendix 1)

$$\vec{B}_n = \frac{5\mu_0}{16\pi R^3}\vec{\mu}_n \tag{3}$$

and

$$\vec{B}_e = \frac{5\mu_0}{16\pi R^3}\vec{\mu}_e, \tag{4}$$

where μ_0 is the vacuum permeability ($4\pi \times 10^{-7}$ H/m) and R is the van der Waals atomic radius (2.75×10^{-10} m) [29]. Chiefly because the nucleus is more massive, μ_e (9.285×10^{-24} J/T) $\gg$ μ_n (1.977×10^{-27} J/T); thus, B_e (558.1×10^{-4} T) $\gg$ B_n (0.119×10^{-4} T), where 10^{-4} T = 1 Gauss.

CQD refers to $\vec{\mu}_e$ as the principal quantum and $\vec{\mu}_n$ in the same atom as the co-quantum. Postulate 1 states that induction between the electron and the nucleus tends to increase $|\theta_e - \theta_n|$, where θ denotes the polar angle relative to the quantization axis (see Paragraph 1 in Discussion). We (1) apply the Landau–Lifshitz–Gilbert equation to both $\hat{\mu}_e$ and $\hat{\mu}_n$, (2) express the unit vectors in spherical coordinates, and (3) revise the signs of the induction terms to implement the above postulate, leading to the following CQD equations of motion (Appendix 2):

$$\dot{\theta}_e = -\gamma_e\left[B_y \cos\phi_e + B_n \sin\theta_n \sin(\phi_n - \phi_e)\right] - \operatorname{sgn}(\theta_n - \theta_e)k_i\left|\dot{\phi}_e\right| \sin\theta_e, \tag{5}$$

$$\dot{\theta}_n = -\gamma_n\left[B_y \cos\phi_n + B_e \sin\theta_e \sin(\phi_e - \phi_n)\right] - \operatorname{sgn}(\theta_e - \theta_n) k_i \left|\dot{\phi}_n\right| \sin\theta_n, \tag{6}$$

$$\dot{\phi}_e = -\gamma_e\left\{B_z + B_n \cos\theta_n - \cot\theta_e \left[B_y \sin\phi_e + B_n \sin\theta_n \cos(\phi_n - \phi_e)\right]\right\} - \frac{\operatorname{sgn}\dot{\phi}_e k_i |\dot{\theta}_e|}{\sin\theta_e}, \tag{7}$$

and

$$\dot{\phi}_n = -\gamma_n\left\{B_z + B_e \cos\theta_e - \cot\theta_n \left[B_y \sin\phi_n + B_e \sin\theta_e \cos(\phi_e - \phi_n)\right]\right\} - \frac{\operatorname{sgn}\dot{\phi}_n k_i |\dot{\theta}_n|}{\sin\theta_n}. \tag{8}$$

Here, ϕ denotes the azimuthal angle; B_y and B_z represent, respectively, the y (axis of the atomic beam) and z components of the external magnetic flux densities; B_x is neglected for brevity; sgn denotes the sign function. When $\theta_e = 0$ or π, Eq. 7 is replaced with $\dot{\phi}_e = 0$; when $\theta_n = 0$ or π, Eq. 8 is replaced with $\dot{\phi}_n = 0$. Primarily because the nucleus is more massive again, γ_e (-1.761×10^{11} rad Hz/T) in absolute value is four orders of magnitude greater than γ_n (1.250×10^{7} rad Hz/T). If $B_n = 0$ and $k_i = 0$, Eq. 5 and 7 reduce to the equations shown by Majorana [10, 11].

CQD branching condition

Postulate 2 states that the polar angle of the co-quantum, θ_n, varies negligibly ($\ll \pi$) during flight in typical Stern–Gerlach experiments, where the duration is too short for the co-quantum to collapse (see Paragraph 2 in Discussion). The external main field, B_0, along the z axis is usually much stronger than B_e and B_n. While the fast motion of $\hat{\mu}_e$ is precession about the main field, the secondary motion is collapse due to the induction term, which yields the following trend from Eq. 5:

$$\tan\frac{\theta_e(t)}{2} = \tan\frac{\theta_e(0)}{2}\exp[-\operatorname{sgn}(\theta_n - \theta_e) k_i |\Delta\phi_e(t)|]. \tag{9}$$

Here, $\Delta\phi_e$ denotes the traversed azimuthal angle (i.e., unwrapped phase). If the Larmor frequency of the electron magnetic moment ω_e is constant, we simply have $\Delta\phi_e = \omega_e t$. As time evolves, θ_e approaches either 0 or π according to the following branching condition:

$$\operatorname{sgn}(\theta_n - \theta_e) = \begin{cases} 1 & \text{if } \theta_n > \theta_e, \\ 0 & \text{if } \theta_n = \theta_e, \\ -1 & \text{else.} \end{cases} \tag{10}$$

Therefore, $\hat{\mu}_e$ collapses to either $+z$ or $-z$ while precessing about B_0, depending on the polar angle of the co-quantum θ_n relative to θ_e (Fig. 2).

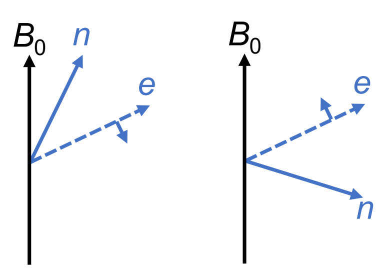

Fig. 2. Examples of collapse directions determined by the branching condition in Stern–Gerlach experiments. B_0: external main field; e: electron magnetic moment (principal quantum), $\hat{\mu}_e$; n: nuclear magnetic moment (co-quantum), $\hat{\mu}_n$; Short arrows: collapse directions. While $\hat{\mu}_e$

precesses about B_0 right-handedly at its Larmor frequency ($\omega_e = -\gamma_e B_0$), $\hat{\mu}_n$ does left-handedly at the Larmor frequency ($\omega_n = -\gamma_n B_0$); note that $|\omega_e/\omega_n| > 10^4$. For the same given $\hat{\mu}_e$, the collapse direction, down (left panel) or up (right panel), depends on $\hat{\mu}_n$ according to the branching condition (Eq. 10). It takes on the order of N_c (estimated to be on the order of ~220 in Results) Larmor cycles to collapse. In typical Stern–Gerlach experiments, it is assumed that $\hat{\mu}_n$ does not collapse, i.e., θ_n is approximately constant.

The number of precession cycles required to vary $\tan(\theta_e/2)$ by a factor of e is given by

$$N_c = \frac{1}{2\pi k_i} \tag{11}$$

regardless of the strength of the external magnetic field. For a constant Larmor frequency, ω_e, the collapse time constant is

$$T_c = N_c \frac{2\pi}{|\omega_e|} = \frac{1}{k_i|\omega_e|}. \tag{12}$$

CQD pre-collapse state function and CQD prediction expression

The CQD pre-collapse state function is denoted by $|\hat{\mu}_e©\hat{\mu}_n\rangle$, where the co-quantum, $\hat{\mu}_n$, is prefixed with © for clarity. $|\hat{\mu}_e©\hat{\mu}_n\rangle$ represents $\hat{\mu}_e$ accompanied with $\hat{\mu}_n$, both governed by the CQD equations of motion.

The CQD prediction expression for Stern–Gerlach experiments is written as

$$|\hat{\mu}_e©\hat{\mu}_n\rangle = C_+(\hat{\mu}_e,\hat{\mu}_n)|+z\rangle + C_-(\hat{\mu}_e,\hat{\mu}_n)\exp(i\phi_e)\,|-z\rangle. \tag{13}$$

The equal sign functions as a right arrow (→) because the right side predicts the measurement outcome. A given $\hat{\mu}_e$ collapses to either $+\hat{z}$ or $-\hat{z}$ according to the branching condition (Eq. 10). The two real and positive C coefficients take on mutually exclusive binary values while $\exp(i\phi_e)$ captures the phase information. If $\theta_n > \theta_e$, then $C_+ = 1$ and $C_- = 0$; if $\theta_n < \theta_e$, $C_+ = 0$ and $C_- = 1$. In either case, $C_+ \cdot C_- = 0$ and $C_+ + C_- = 1$.

3. Results

Single-stage Stern–Gerlach experiment

To describe the angular distribution of $\hat{\mu}_e$ or $\hat{\mu}_n$ in an ensemble of atoms, we define the angular probability density function, $p(\theta,\phi)$, as the probability of $\hat{\mu}$ pointing to the vicinity of (θ,ϕ) per unit infinitesimal solid angle, with the following normalization:

$$\int_0^{\pi}\int_0^{2\pi} p(\theta,\phi)\sin\theta\,d\phi\,d\theta = 1. \tag{14}$$

If the azimuthal distribution is isotropic, the integral reduces to $\int_0^{\pi} p(\theta,\phi)2\pi\sin\theta\,d\theta = 1$.

The angular distribution of $\hat{\mu}_n$ for atoms immediately out of the oven is presumed to be isotropic as given by (Fig. 3, Inset a, dashed circle)

$$p_{n0}(\theta_n,\phi_n) = \frac{1}{4\pi}. \tag{15}$$

In a single-stage Stern–Gerlach experiment (Fig. 3, SG1), the probabilities of collapse for a given θ_e are related to the binary coefficients through ensemble averaging of the pre-averaging density operator defined in Appendix 3 (Eq. 70) over p_{n0}. The outcome is summarized as

$$\langle C_+\rangle_n^2 = \int_{\theta_e}^{\pi} p_{n0} 2\pi \sin\theta_n \, d\theta_n = \cos^2\frac{\theta_e}{2} \tag{16}$$

and

$$\langle C_-\rangle_n^2 = \int_0^{\theta_e} p_{n0} 2\pi \sin\theta_n \, d\theta_n = \sin^2\frac{\theta_e}{2}. \tag{17}$$

The angle brackets, with the subscripts denoting nuclear, represent ensemble averaging with the integration limits determined by the branching condition (Eq. 10). The two probabilities are proportional to the solid angles formed by the down and up sides of the cone shaped by the initial Bloch vector [15] precessing over one cycle. Each solid angle determines the probability of having the co-quantum on the corresponding side of the cone.

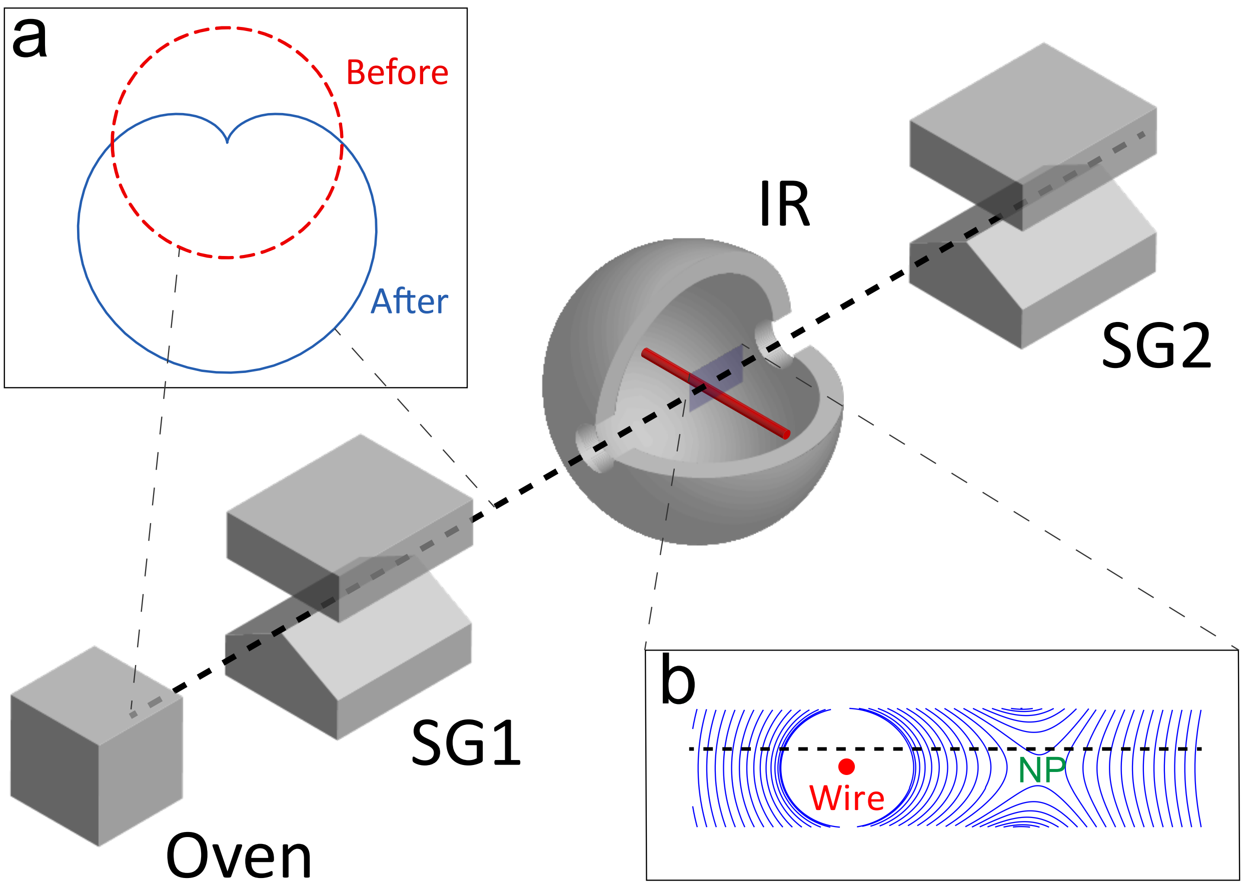

Fig. 3. Multi-stage Stern–Gerlach (SG) experiment conducted by Frisch and Segrè [9]. The atomic beam from the oven is sent through (1) Stage SG1 to collapse $\hat{\mu}_e$ (principal quantum), (2) the magnetically shielded inner rotation (IR) chamber to rotate $\hat{\mu}_e$, (3) a slit (not shown) to select a branch, and (4) Stage SG2 to measure the fraction of spin flip. The red solid line and filled circle represent the current-carrying wire, and the gray sphere in cutaway view represents magnetic shielding. **Inset (a)** Angular distributions of $\hat{\mu}_n$ (co-quanta) before and after Stage SG1. **Inset (b)**

Magnetic field lines within the IR chamber; NP: null point, formed by the cancelation of the magnetic field from the wire by the vertical remnant (residual) fringe magnetic field. Here, the vertical distance of the atomic beam from the center of the wire, $z_a = 1.05 \times 10^{-4}$ m; the most likely speed of atoms, $v = 800$ m s^{-1}; the uniformly distributed remnant (residual) fringe magnetic flux density, $B_r = 0.42 \times 10^{-4}$ T, which is parallel with the $+z$ axis (up in the figure); and the current carried by the wire, I, points along the $-x$ axis (into the screen).

From Eq. 16 and 17, the pre-collapse state function (Eq. 13) averages to the following familiar quantum mechanical wave function for a pure state (Appendix 3):

$$|\hat{\mu}_e\rangle = \cos\frac{\theta_e}{2}|+z\rangle + \sin\frac{\theta_e}{2}\exp(i\phi_e)\,|-z\rangle. \tag{18}$$

If $\hat{\mu}_e$ is also isotropically distributed as

$$p_{e0}(\theta_e, \phi_e) = \frac{1}{4\pi}, \tag{19}$$

the probabilities of collapse are predicted by averaging Eq. 16 and 17 over p_{e0} (Appendix 3):

$$\langle C_+\rangle_{n,e}^2 = \int_0^\pi \cos^2\frac{\theta_e}{2} p_{e0} 2\pi \sin\theta_e \, d\theta_e = \frac{1}{2} \tag{20}$$

and

$$\langle C_-\rangle_{n,e}^2 = \int_0^\pi \sin^2\frac{\theta_e}{2} p_{e0} 2\pi \sin\theta_e \, d\theta_e = \frac{1}{2}. \tag{21}$$

The e subscripts denote electron. The outcomes agree with the familiar quantum mechanical prediction for a maximally mixed state of atoms immediately out of the oven, represented by a density operator (Eq. 87, Appendix 3).

Multi-stage Stern–Gerlach experiment

In the multi-stage Stern–Gerlach experiment conducted by Frisch and Segrè (Fig. 3) [9], Stage SG1 collapses $\hat{\mu}_e$ into two branches. The inner rotation (IR) chamber rotates $\hat{\mu}_e$ by an angle of α_r using the magnetic field shown in Inset b. A slit (not shown) selects one branch: the $+z$ branch is chosen here. Stage SG2 collapses $\hat{\mu}_e$ and measures the fraction of spin flip. Therefore, Stage SG1 serves as a polarizer, the IR chamber a rotator, and Stage SG2 an analyzer.

The probability of spin flip has been predicted [10, 11] by quantum mechanics as (see Eq. 17, set $\theta_e = \alpha_r$)

$$W_{\text{qm}} = \langle -z|\alpha_r\rangle^2 = \sin^2\frac{\alpha_r}{2}, \tag{22}$$

which leads to the following Majorana formula (Appendix 4, Eq. 117) [10, 11]:

$$W_m = \exp\left(-\frac{\pi z_a}{2v}|\gamma_e|B_y\right). \tag{23}$$

Here, z_a is the vertical distance of the atomic beam from the center of the wire, and v is the most likely speed of the atoms. The spin flip is because B_z vanishes and reverses its sign near the null point (Fig. 3, Inset b). Because B_y is inversely proportional to the current carried by the wire, I (Eq. 92 and 94 in Appendix 4), the Majorana formula predicts a probability of spin flip approaching 100% with increasing currents (Fig. 4, Curve m), i.e., as $B_y \to 0$, $W_m \to 1$; yet, the experimental outcome decreases to nearly zero after peaking at 31% (Fig. 4, circles) [9]. Consequently, W_m yields a negative coefficient of determination (R^2). Using the dimensionless adiabaticity parameter k_m (Eq. 103 in Appendix 4), one can express the above equation concisely as $W_m = \exp(-\pi k_m/2)$ (Eq. 116). Rabi revised the Majorana formula to $W_m^{1/4}/4$ [16], which, however, overestimates the starting points, underestimates the peak, and continues to diverge thereafter; as a result, the R^2 remains negative (Fig. 1).

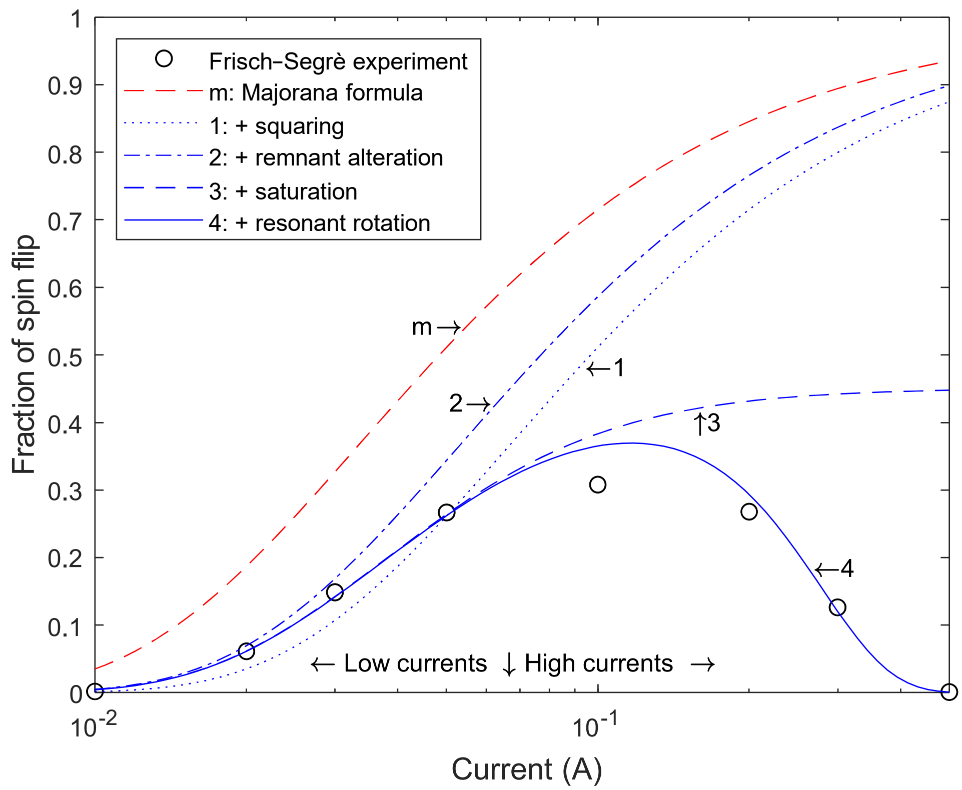

Fig. 4. Fraction of spin flip versus wire current. The down arrow points to the current where $B'_y = B_n \sin\langle\theta_n\rangle$ or $k_0 = k_1$ to separate the low- and high-current regions. Curves m and 1–4 represent W_m and $W_1 - W_4$, respectively. While W_m diverges from the experiment with a negative R^2, W_3 matches the low-current experimental observation in absolute units without fitting with $R^2 = 0.9495$; further, W_4 matches the entire observation with improved $R^2 = 0.9787$ and $p < 8 \times 10^{-7}$. No adjustable or free parameters are used.

In CQD, Stage SG1 varies θ_n negligibly according to Postulate 2. However, polarization selection by the slit reshapes the co-quantum angular distribution from the original isotropic p_{n0} (Eq. 15) to

$$p_{n1}(\theta_n, \phi_n) = p_{n0}(\theta_n, \phi_n) \cdot 2\int_0^{\theta_n} p_{e0} 2\pi \sin\theta_e \, d\theta_e = \frac{1-\cos(\theta_n)}{4\pi}. \tag{24}$$

Here, the pre-factor 2 compensates for the overall slit rejection of the opposite polarization (Eq. 20), p_{e0} is given by Eq. 19, and the integration limits are based on the branching condition (Eq. 10). Because atoms with smaller θ_n are deflected to the blocked $-z$ branch with greater probabilities, p_{n1} forms a heart shape (Fig. 3, Inset a, solid line; Paragraph 3 in Discussion).

The heart shape is assumed to be approximately maintained throughout the inner rotation chamber owing to the extension of Postulate 2 (see Paragraph 2 in Discussion). The co-quanta engender the following four effects on the principal quanta.

First, the probability of spin flip is derived by ensemble averaging over p_{n1} instead of p_{n0} (Eq. 89 with $\theta_e = \alpha_r$ in Appendix 3):

$$W_{\text{cqd}} = \langle -z|\alpha_r\rangle^2 = \int_0^{\alpha_r} p_{n1} 2\pi \sin\theta_n \, d\theta_n = \sin^4\left(\frac{\alpha_r}{2}\right), \tag{25}$$

which equals W_{qm}^2 (Eq. 22). As shown by Curve 1 in Fig. 4, simply squaring W_m (Eq. 23) already brings the solution much closer to the observation at low currents, but with an overcorrection near $I = 0.03$ A. This squaring effect evolves the probability of spin flip from W_m to

$$W_1 = W_m^2 = \exp\left(-\frac{\pi z_a}{v}|\gamma_e|B_y\right), \tag{26}$$

where B_y is computed from the remnant (residual) fringe magnetic flux density, B_r, using Eq. 92 and 94 in Appendix 4. Using the dimensionless adiabaticity parameter k_m (Eq. 103), one can express the above equation concisely as $W_1 = \exp(-\pi k_m)$ (see Eq. 154 in Appendix 5).

Second, the z component of $\vec{B}_n$ (Eq. 3), represented by $B_n \cos\langle\theta_n\rangle$, offsets the upward B_r. We substitute $B_r + B_n \cos\langle\theta_n\rangle$ (Eq. 119 in Appendix 5) for B_r to update B_y to B_y' (Eq. 122). The heart shape (Eq. 24) yields $\langle\theta_n\rangle = 5\pi/8$ (Eq. 118). The magnitude of $B_n \cos\langle\theta_n\rangle = -0.045 \times 10^{-4}$ T exceeds 10% of B_r (0.42×10^{-4} T), producing an appreciable remnant-alteration effect. As shown by Curve 2 in Fig. 4, the corrected curve passes through the first two data circles and grazes the third one. If the co-quantum distribution were isotropic, $\langle\theta_n\rangle$ would be $\pi/2$; $B_n \cos\langle\theta_n\rangle$ would vanish, so would the remnant-alteration effect. Effect 2 evolves W_1 to (see Eq. 136)

$$W_2 = \exp\left(-\frac{\pi z_a}{v}|\gamma_e|B_y'\right), \tag{27}$$

where B_y', however, is computed using $B_r + B_n \cos\langle\theta_n\rangle$ instead of B_r. Using the dimensionless adiabaticity parameters k_0 (Eq. 125), one can express the above equation concisely as $W_2 = \exp(-\pi k_0)$ (see Eq. 153).

Third, the co-quanta saturate the rotation. As shown by Eq. 27, W_2 increases with decreasing B_y'. However, the weakness of B_y' is spoiled by the transverse (xy) component of $\vec{B}_n$, denoted by $B_n \sin\langle\theta_n\rangle$. Substitution of $\sqrt{B_y'^2 + (B_n \sin\langle\theta_n\rangle)^2}$ for B_y' (see Eq. 141) evolves W_2 to

$$W_3 = \exp\left(-\frac{\pi z_a}{v}|\gamma_e|\sqrt{B_y'^2 + (B_n \sin\langle\theta_n\rangle)^2}\right). \tag{28}$$

Using the dimensionless adiabaticity parameters k_0 (Eq. 125) and k_1 (Eq. 126), one can express the above equation concisely as $W_3 = \exp\left(-\pi\sqrt{k_0^2 + k_0 k_1}\right)$ (see Eq. 152).

As shown by Curve 3 in Fig. 4, this rotation-saturation effect clamps the overshoot in Curve 2. The clamped curve passes through the first four data circles. The current is divided into two regions at 0.067 A, where $B_y' = B_n \sin\langle\theta_n\rangle = 0.11 \times 10^{-4}$ T. At low currents before the fourth data point ($I = 0.05$ A and $B_y' = 0.15 \times 10^{-4}$ T), B_y' is greater than $B_n \sin\langle\theta_n\rangle$; at high currents, conversely, $B_n \sin\langle\theta_n\rangle$ becomes dominant and saturates the curve. If the co-quantum distribution were isotropic, then $\langle\theta_n\rangle = \pi/2$; consequently, both the squaring and remnant-alteration effects (effects 1 and 2) would vanish. In this case, the rotation-saturation effect (effect 3) alone could not bring the Majorana solution down sufficiently in the low-current region because as the current decreases B'_y increasingly overpowers B_n; thus, the effect of the co-quanta would become negligible.

Combining the three effects, CQD accurately predicts the low-current observation in absolute units without fitting (i.e., no parameters are adjusted). The coefficient of determination R^2 for the low-current regime reaches 0.9495 as computed using the natural logarithm of the fractions of flip to suppress the exponential dependence (Eq. 28). Therefore, effecting the three modifications to the Majorana formula has already shown evidence for the existence of both the co-quantum and the derived heart-shaped distribution.

Fourth, in the high-current regime, the precession of $\vec{B}_n$ generates substantial nuclear-resonant rotation, due to precession resonance between $\vec{\mu}_e$ and $\vec{\mu}_n$ when their Larmor frequencies are matched (see Appendix 5 for details). This effect evolves W_3 to (Eq. 167 in Appendix 5)

$$W_4 = W_3 \exp(-c_{r1} I^3), \tag{29}$$

where the resonant-rotation coefficient, c_{r1}, is given by Eq. 163. The fraction of spin flip peaks near $I = 0.1$ A, where $B'_y = 0.074 \times 10^{-4}$ T, comparable to but less than $B_n \sin\langle\theta_n\rangle = 0.11 \times 10^{-4}$ T. As shown by Curve 4 in Fig. 4, this effect increases with the current and bends down Curve 3. At the maximum current ($I = 0.5$ A), $B'_y = 0.015 \times 10^{-4}$ T, far less than $B_n \sin\langle\theta_n\rangle$; the fraction of spin flip decreases to nearly zero. Expression of the above equation based on dimensionless parameters is discussed below Eq. 150. Using the dimensionless adiabaticity parameters k_0 (Eq. 125) and k_1 (Eq. 126) as well as f_{r1} (Eq. 146), one can express the above equation concisely as $W_4 = \exp\left(-\pi\sqrt{k_0^2 + k_0 k_1} - \frac{1}{2}[\pi k_1]^2 f_{r1}\right)$ (see Eq. 151), where f_{r1} denotes the fraction of the Larmor period of the nuclear magnetic moment precessed during the effective flight path-length for nuclear-resonant rotation.

Combining all four effects, CQD accurately predicts the experimental observation in absolute units without fitting (Fig. 4, Curve 4) over the entire domain; R^2 is computed to be 0.9787 using the natural logarithm of the fractions of flip to suppress the exponential dependence (Eq. 29). Under the null hypothesis that the theoretical prediction is uncorrelated with the observation, we estimate the p-value to be $< 8 \times 10^{-7}$ (Function *regress* or *corr*, MATLAB, MathWorks) [22, 23]. Such a small p-value further objectively confirms the existence of both the co-quantum and the derived heart-shaped distribution. In comparison, without taking the logarithm of the fractions of flip, R^2 is computed to be 0.9621.

Thus far, we have set the induction factor $k_i = 0$ for the flight in the inner rotation chamber, owing to the low field (Appendix 5). Including k_i yields the following combined probability of spin flip (Appendix 5, Eq. 160):

$$W_{\mathrm{cqd}} = \exp\left[-\sqrt{(c_{r0}/I)^2 + c_{rs}^2} - c_{r1} I^3 - c_{ri} I\right], \tag{30}$$

where c_{r0}, c_{rs}, c_{r1}, and c_{ri} represent null-point rotation, rotation saturation, nuclear-resonant rotation, and induction rotation, respectively. The current, I, controls the external magnetic field in the inner rotation chamber. Taken from Frisch and Segrè [9], the only device-specific parameters for the predictions include B_r (0.42×10^{-4} T), z_a (1.05×10^{-4} m), and v (800 m s^{-1}). The theoretical predictions from Eq. 161–163 without adjusting any parameters are c_{r0} = 0.054 A, c_{rs} = 0.80, and c_{r1} = 48 A^{-3}. Substitution of these coefficients into Eq. 30 with $c_{ri} = 0$ produces Curve 4 in Fig. 4, where no free parameters are used.

Despite its small contribution in the inner rotation chamber, the induction factor is estimated for its order of magnitude. While holding all three other parameters constant at the predicted values, fitting W_{cqd} (Eq. 30) for the experimental data in Fig. 4 yields $c_{ri}{\sim}0.57$ A. Substitution into Eq. 164 produces $k_i{\sim}7.4 \times 10^{-4}$. Further substitution into Eq. 11 concludes that electron-spin collapse takes on the order of $N_c{\sim}220$ precession cycles.

4. Discussion

CQD postulates that the electron and nuclear magnetic moments in an external field B_0 along z repel in the polar direction, which results in a revision to the sign of the induction term in the Landau–Lifshitz–Gilbert equation. Whereas precession is governed by the terms from the Bloch equation, collapse is modeled by the revised induction term. If $k_i = 0$, the equation of motion reduces to the Bloch or equivalent Schrödinger equation [7, 10, 11, 26, 27], which does not model collapse [30]. While precession is the dominant motion, collapse is secondary but concurrent. Although the exact mechanism for the repulsion is to be investigated, a conjecture is diamagnetism extended from orbital to spin motions. Diamagnetic magnetization, a weak but universal induction effect on all atoms, causes repulsion [31, 32]. The relativistic momentum density in the Dirac wave field shows that the magnetic moment of an electron can be attributed to a circulating flow of electric charge (Eq. 34 in Appendix 1), similar to that in orbital motions [33]. Therefore, it is conceivable that diamagnetism applies to spin as well. In the laboratory reference frame, as $\vec{\mu}_e$ and $\vec{\mu}_n$ precess in opposite directions, each azimuthal encounter may be viewed as a "collision", causing repulsion. Because induction is related to relative motion, the induced field on the electron may be written as $\vec{B}_i \propto d(\hat{\mu}_e - \hat{\mu}_n)/dt$, and the corresponding induced torque is $\vec{\tau}_i \propto \hat{\mu}_e \times \vec{B}_i$. If $\hat{\mu}_e \times d\hat{\mu}_n/dt$ averages out, the average induced torque becomes $\hat{\mu}_e \times d\hat{\mu}_e/dt$, matching the induction term in the Landau–Lifshitz–Gilbert equation. As $\hat{\mu}_e$ nears either up or down, the average induced torque approaches zero, providing stability. In the rotating reference frame that rotates at ω_e, the external B_0 vanishes, $\vec{\mu}_e$ becomes azimuthally stationary [34]; the rapidly precessing $\vec{\mu}_n$ forms in the time-average sense a cone-shaped magnet, which repels $\vec{\mu}_e$ towards $\pm z$. The sign function in the induction terms in the equations of motion is the key difference from the standard Landau–Lifshitz–Gilbert equation and is central to CQD. While standard damping always leads to a lower-energy state, collapse due to the co-quantum can reach a state of either higher or lower energy in the presence of an external magnetic field, according to the branching condition, which agrees with the Stern–Gerlach experimental observation. Numerical solutions to the CQD equations of motion, to be reported separately, have illustrated collapse with the induction term and none without. This postulate is consistent with the Pauli exclusion principle for two identical fermions, where the two magnetic moments repel towards anti-alignment. Therefore, one may regard this postulate as an extension to the Pauli exclusion principle. Note that while diamagnetism explains the collapse term, paramagnetism is expected to perturb the precession term slightly, which is neglected here.

CQD also postulates that the polar angle of $\vec{\mu}_n$ in flight varies negligibly. Because the nuclear Larmor frequency is four orders of magnitude smaller (i.e., $|\omega_n| \ll |\omega_e|$), nuclear spin collapses much more slowly than electron spin. Because no data on the collapse rates have been found in the literature, we reference the T_1 relaxation times. Typical T_1 relaxation times in electron paramagnetic resonance are on the μs scale [35], consistent with the previous estimation of the collapse time scale of $\vec{\mu}_e$ [5]. In contrast, typical T_1 relaxation times in gas-phase nuclear magnetic resonance are on the ms scale [36], indicating the order-of-magnitude collapse time of $\vec{\mu}_n$. In a typical Stern–Gerlach experiment [5, 37], the main external field B_0 along z is at least 0.3 T ($B_0 > B_e \gg B_n$, the Paschen–Back regime [16]), the length of the main field is ~35 mm, and the most likely atomic speed v is ~800 m s^{-1}. Consequently, the flight time through the main field is only ~44 μs, which is long enough for $\vec{\mu}_e$ to collapse but too short for $\vec{\mu}_n$ to collapse. In fact, the fringe field on the source side of the main field collapses $\vec{\mu}_e$ [2]. Besides the two distinct collapse branches due to the quantization of $\vec{\mu}_e$, no additional branches due to the quantization of $\vec{\mu}_n$ have been observed by Frisch and Segrè [9] despite the prediction of up to eight branches total [38]. For N_c~220 (Eq. 11) estimated from the Frisch–Segrè experimental data shown in Fig. 4, the collapse time constants (T_c, Eq. 12 and its nuclear counterpart) at the main field strength are computed to be ~3×10^{-8} and ~4×10^{-4} s for $\vec{\mu}_e$ and $\vec{\mu}_n$, respectively, which are consistent with the above-mentioned corresponding T_1 relaxation times in orders of magnitude [35] [36]. This postulate, extended to the weaker-field inner rotation chamber, is consistent with the selection rule for observing an electron-spin–resonance transition, stating that the magnetic quantum number of the nuclear spin remains constant (i.e., $\Delta m_I = 0$) [39]. The selection rule was also a major basis for Rabi's revision to the Majorana formula [16].

The heart-shaped p_{n1} in Eq. 24 (Fig. 3, Inset a) can be understood in two ways. First, the integral can be perceived as the expected transmittance through Stage SG1 for a given θ_n. All principal quanta with $\theta_e < \theta_n$ collapse to $+z$, and the atoms propagate through the slit further; otherwise, the atoms are blocked by the slit. The greater the θ_n is, the greater the transmittance, proportional to the solid angle formed by the cone having a half angle of θ_n (Fig. 5). Second, one may examine how much principal quanta at the source around each θ_e within $d\theta_e$ contribute to p_{n1}. For $\theta_e = 0$, the contribution forms a perfect spherical distribution of co-quanta because co-quanta in any direction can reach the second stage. For $0 < \theta_e < \pi$, the contribution forms a truncated sphere with the cone of $\theta_n < \theta_e$ removed because co-quanta in this range have collapsed the principal quanta to the blocked branch. For $\theta_e = \pi$, the contribution vanishes because the principal quanta are always in the blocked branch. Integrating these (truncated) spheres form the final heart shape. Conversely, the co-quantum angular distribution for the opposite branch is an inverted heart shape. Average the two complementary shapes recovers the original isotropic p_{n0}.

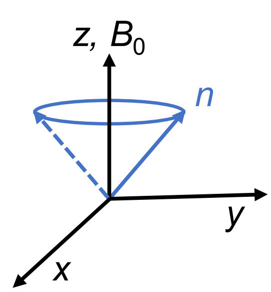

Fig. 5. Illustration of the cone of $\hat{\mu}_n$ formed by precession around the external main field, B_0. n: nuclear magnetic moment (co-quantum), $\hat{\mu}_n$. Any electron magnetic moment (principal quantum), $\hat{\mu}_e$, precessing around B_0 within the cone collapses up, whereas $\hat{\mu}_e$ precessing outside the cone

collapses down. For a given θ_n, the probability for the atom from the oven to reach the up branch in the single-stage Stern–Gerlach experiment is proportional to the solid angle of the cone.

A key reason for the agreement between CQD and the Frisch–Segrè experimental observation is that the angular distribution of the co-quantum (i.e., the nuclear magnetic moment) is changed from an isotropic shape (Eq. 15) to a continuous heart shape (Eq. 24) due to the polarization. The subsequent effects are illustrated using the evolution of the curves in Fig. 4. As more effects are included, the model becomes more and more accurate while all parameters were given (i.e., no parameters were tuned to fit the experimental data). If the heart shape were incorrect, the agreement would be completely off. In comparison, the Majorana or Landau–Zener formula neglected the nuclear magnetic moment altogether, and Rabi used an isotropic angular distribution instead of the heart shape [16]. Note that as the wire current approaches infinity, Rabi's formula predicts a maximum of $\frac{1}{2I+1} = \frac{1}{4}$, which is well below the experimental peak of 31% (Fig. 1); here, $I = \frac{3}{2}$ denotes the nuclear spin number for potassium-39. Further, Rabi's standard hyperfine coupling does not contain the induction terms in CQD and hence does not model collapse. Also, the torque-averaged fields provide greater agreement than the self-averaged fields (see Appendix 1).

Quantum mechanics, celebrated for its countless triumphs, still pose mysteries as discussed insightfully in recent literature [30, 40-43]. The Copenhagen interpretation construes that an electron spin is simultaneously in both eigenstates and collapses statistically upon measurement to either [7]. The collapse is not modeled by the original Schrödinger equation but stated separately as a measurement postulate [30]. Debatable inconsistency has been found in thought experiments, such as "Schrödinger's cat" [44-46].

CQD potentially offers new insight. If co-quanta are isotropically distributed, CQD has been verified with quantum mechanics by exactly reproducing the wave function and the density operator (Appendix 3) as well as the uncertainty relation (Appendix 6) and entangled wave function (Appendix 7). The probabilities of reaching the two eigenstates split according to $\cos^2\frac{\theta_e}{2} : \sin^2\frac{\theta_e}{2}$; the wave function is reproduced in Eq. 18. However, if the co-quanta have, for example, a heart-shaped distribution (Eq. 24), the split becomes $1 - \sin^4\frac{\theta_e}{2} : \sin^4\frac{\theta_e}{2}$ (Eq. 88 and 89 in Appendix 3); the wave function is revised accordingly (Eq. 90). The density operator is found to originate from a pre-averaging counterpart with independent realizations (Appendix 3). The measurement uncertainty product, explained by co-quanta, depends on the initial phase of the principal quanta and the measurement sequence, as shown by the uncertainty equality (Eq. 186), which leads to the familiar quantum mechanical inequality (Eq. 187). CQD has also enabled the derivation from the classical Bloch equation to the quantum Schrödinger–Pauli equation [17], while the latter has thus far been treated as a postulate.

CQD can be further tested with atoms having nuclear spins of 0 ($\mu_n = 0$), which may collapse differently in Stern–Gerlach experiments. A natural question is whether higher-order nuclear multipoles could serve as co-quanta. Examples include ^{38m1}K, ^{50}K, ^{94}Ag, and ^{130}Ag, which are isotopes of the stable ^{39}K, ^{107}Ag, and ^{109}Ag. Unfortunately, these isotopes have short lifetimes ranging from 100s to 10s of ms. Note that free electrons have not been used owing to the Lorentz force and orbital magnetic moment.

Since the submission of this manuscript, our team has produced several new manuscripts to support this work. Titimbo et al. numerically modeled the Frisch–Segrè experiment using CQD via the Bloch equation [47], whereas He et al. numerically modeled the experiment using CQD via the Schrödinger equation [48]. Both works have numerically confirmed the analytical solution presented here and the equivalence between the the Bloch equation and the Schrödinger equation stated by Majorana. Interestingly, Majorana wrote the "Bloch" equation [10, 11] fourteen years before Bloch published his eponymous equation [49]. The author recently derived from the Bloch equation, which Bloch intended for macroscopic magnetization instead of individual nuclear magnetic moments [49], to the Schrödinger or Schrödinger–Pauli equation [17]. Kahraman et al. demonstrated that the standard existing treatment of hyperfine interaction, consistent with the Breit–Rabi formula [38], cannot model the Frisch–Segrè experiment accurately but can be improved by incorporating CQD features [50]. The treatment also does not agree with the Rabi formula [16].

While no alternative theory, to the best of our knowledge, matches the Frisch–Segrè experiment, a recent multi-stage Stern–Gerlach experiment on superatomic icosahedral cage-clusters Mn@Sn_{12} also reveals discrepancy of the Landau–Zener formula from experimental observation [51].

5. Conclusions

CQD, based on the sign-modified Landau–Lifshitz–Gilbert equation, provides a plausible collapse mechanism for electron spin in Stern–Gerlach experiments. CQD models both spin evolution and collapse by the same equations of motion. With an anisotropic angular distribution of co-quanta, CQD revises the wave function and accurately predicts the Frisch–Segrè experimental observation in absolute units without fitting with adjustable parameter, achieving $p < 8 \times 10^{-7}$—an objective statistical indication that reflects both correlation and degrees of freedom. Therefore, it is extremely unlikely that CQD happens to match the experimental observation so well by sheer chance. Further, with an isotropic angular distribution of co-quanta, CQD is theoretically corroborated by quantum mechanics. Both the strong experimental evidence and the exact quantitative agreement with quantum mechanics in diverse forms collectively support CQD. Like statistical mechanics [52], which uses molecular properties to predict macroscopic properties by ensemble averaging, CQD reproduces quantum mechanical properties by ensemble averaging over co-quanta (Appendix 3). If orthodox quantum mechanics is incomplete [44], CQD may stimulate development for a complete theory.

Acknowledgments

The author thanks Dr. Yixuan Tan for discussing the work, translating the German references using Google Translate, and drawing Fig. 3; Drs. Zhe He and Kelvin Titimbo Chaparro for verifying the mathematical derivations and discussing the manuscript; Yixuan Tan, David Garrett, Kelvin Titimbo Chaparro, Siddik Suleyman Kahraman, and Zhe He for verifying CQD numerically (to be reported); Prof. JT Shen and Mr. Siddik Suleyman Kahraman for discussing the manuscript; Prof. Naisyin Wang and Mr. Sean Wang for discussing the statistics; Dr. Victor Wang for discussing the math; and Prof. James Ballard for editing an early version of the manuscript.

Data availability statement

The data that support the findings of this study are available upon request from the authors.

References

1. Gerlach W, Stern O. Der experimentelle nachweis der richtungsquantelung im magnetfeld. Zeitschrift für Physik. 1922;9(1):349-52. doi: 10.1007/BF01326983.
2. Schmidt-Böcking H, Schmidt L, Lüdde HJ, Trageser W, Templeton A, Sauer T. The Stern-Gerlach experiment revisited. The European Physical Journal H. 2016;41(4):327-64. doi: 10.1140/epjh/e2016-70053-2.
3. Castelvecchi D. The Stern–Gerlach experiment at 100. Nature Reviews Physics. 2022. doi: 10.1038/s42254-022-00436-4.
4. Einstein A, Ehrenfest P. Quantentheoretische bemerkungen zum experiment von Stern und Gerlach. Zeitschrift für Physik. 1922;11(1):31-4. doi: 10.1007/BF01328398.
5. Wennerström H, Westlund P-O. The Stern–Gerlach experiment and the effects of spin relaxation. Physical Chemistry Chemical Physics. 2012;14(5):1677-84. doi: 10.1039/C2CP22173J.
6. Norsen T. The pilot-wave perspective on spin. Am J Phys. 2014;82(4):337-48.
7. Feynman RP, Leighton RB, Sands ML. The Feynman Lectures on Physics. Reading, Mass.: Addison-Wesley Pub. Co.; 1963.
8. Phipps TE, Stern O. Über die einstellung der richtungsquantelung. Zeitschrift für Physik. 1932;73(3):185-91. doi: 10.1007/BF01351212.
9. Frisch R, Segrè E. Über die einstellung der richtungsquantelung. II. Zeitschrift für Physik. 1933;80(9):610-6. doi: 10.1007/BF01335699.
10. Majorana E. Atomi orientati in campo magnetico variabile. Il Nuovo Cimento (1924-1942). 1932;9(2):43-50. doi: 10.1007/BF02960953.
11. Majorana E. Oriented atoms in a variable magnetic field. In: Bassani G, editor. Ettore Majorana: Scientific Papers. Bologna, Berlin: Società Italian die Fisica and Springer; 2006. p. 125-32.
12. Landau L. Zur theorie der energieubertragung. II. Physikalische Zeitschrift der Sowjetunion. 1932;2:46–51.
13. Zener C. Non-adiabatic crossing of energy levels. Proceedings of the Royal Society of London Series A. 1932;137:696.
14. Stueckelberg ECG. Theorie der unelastischen Stösse zwischen atomen. Helvetica Physica Acta. 1932;5:369.
15. Ivakhnenko OV, Shevchenko SN, Nori F. Nonadiabatic Landau–Zener–Stückelberg–Majorana transitions, dynamics, and interference. Physics Reports. 2023;995:1-89. doi: 10.1016/j.physrep.2022.10.002.
16. Rabi II. On the process of space quantization. Physical Review. 1936;49(4):324-8. doi: 10.1103/PhysRev.49.324.
17. Wang LV. Derivation from Bloch Equation to von Neumann Equation to Schrödinger–Pauli Equation. Found Phys. 2022;52(3):61.
18. Carlesso M, Donadi S, Ferialdi L, Paternostro M, Ulbricht H, Bassi A. Present status and future challenges of non-interferometric tests of collapse models. Nature Physics. 2022. doi: 10.1038/s41567-021-01489-5.
19. Ghirardi GC, Rimini A, Weber T. Unified dynamics for microscopic and macroscopic systems. Phys Rev D. 1986;34(2):470-91. doi: 10.1103/physrevd.34.470.
20. Pearle P. Combining stochastic dynamical state-vector reduction with spontaneous localization. Physical Review A. 1989;39(5):2277.
21. Ghirardi GC, Pearle P, Rimini A. Markov processes in Hilbert space and continuous spontaneous localization of systems of identical particles. Physical Review A. 1990;42(1):78-89. doi: 10.1103/physreva.42.78.

22. Steel RGD, Torrie JH. Principles and Procedures of Statistics. New York: McGraw Hill; 1960.
23. Rahman N. A Course in Theoretical Statistics. New York: Charles Griffin and Company; 1968.
24. Cousins RD. The Jeffreys–Lindley paradox and discovery criteria in high energy physics. Synthese. 2017;194(2):395-432.
25. Abbott BP, Abbott R, Abbott TD, Abernathy MR, Acernese F, Ackley K, et al. Observation of Gravitational Waves from a Binary Black Hole Merger. Phys Rev Lett. 2016;116(6). doi: 10.1103/physrevlett.116.061102.
26. Grynberg G, Aspect A, Fabre C. Introduction to Quantum Optics: from the Semi-classical Approach to Quantized Light. Cambridge University Press; 2010.
27. Feynman RP, Vernon Jr FL, Hellwarth RW. Geometrical representation of the Schrödinger equation for solving maser problems. Journal of applied physics. 1957;28(1):49-52.
28. Gilbert TL. A phenomenological theory of damping in ferromagnetic materials. IEEE Transactions on Magnetics. 2004;40(6):3443-9. doi: 10.1109/TMAG.2004.836740.
29. Los Alamos National Laboratory: Periodic Table of Elements. https://periodic.lanl.gov/19.shtml Accessed.
30. Norsen T. Foundations of Quantum Mechanics. Springer; 2017.
31. Griffiths DJ. Introduction to Electrodynamics. 4th ed. Cambridge University Press; 2017.
32. Jackson JD. Classical Electrodynamics. USA: John Wiley & Sons; 1999.
33. Ohanian HC. What is spin? Am J Phys. 1986;54(6):500-5. doi: 10.1119/1.14580.
34. Rabi II, Ramsey NF, Schwinger J. Use of rotating coordinates in magnetic resonance problems. Reviews of Modern Physics. 1954;26(2):167.
35. Forbes MD, Jarocha LE, Sim S, Tarasov VF. Time-resolved electron paramagnetic resonance spectroscopy: History, technique, and application to supramolecular and macromolecular chemistry. In: Williams IH, Williams NH, editors. Advances in Physical Organic Chemistry. Elsevier; 2013. p. 1-83.
36. Marchione AA, Conklin B. Gas Phase NMR for the Study of Chemical Reactions: Kinetics and Product Identification. In: Jackowski K, Jaszuński M, editors. Gas Phase NMR. Cambridge: Royal Society of Chemistry; 2016. p. 126-51.
37. Schroder W, Baum G. A spin flipper for reversal of polarisation in a thermal atomic beam. Journal of Physics E: Scientific Instruments. 1983;16(1):52.
38. Breit G, Rabi I. Measurement of nuclear spin. Physical Review. 1931;38(11):2082.
39. Barra AL, Hassan AK. Electron Spin Resonance. In: Bassani F, Liedl GL, Wyder P, editors. Encyclopedia of Condensed Matter Physics. Oxford: Elsevier; 2005. p. 58-67.
40. Adler SL, Bassi A. Is Quantum Theory Exact? Science. 2009;325(5938):275-6. doi: doi:10.1126/science.1176858.
41. Bricmont J. Making Sense of Quantum Mechanics. Springer; 2016.
42. Laloë F. Do We Really Understand Quantum Mechanics? Cambridge University Press; 2019.
43. Auletta G. The Quantum Mechanics Conundrum: Interpretation and Foundations. Springer; 2019.
44. Einstein A, Podolsky B, Rosen N. Can quantum-mechanical description of physical reality be considered complete. Physical Review. 1935;47(10):777-80. doi: 10.1103/PhysRev.47.777.
45. Frauchiger D, Renner R. Quantum theory cannot consistently describe the use of itself. Nature Communications. 2018;9(1):3711. doi: 10.1038/s41467-018-05739-8.
46. Schrödinger E. Die gegenwärtige situation in der quantenmechanik. Naturwissenschaften. 1935;23:807.

47. Titimbo K, Garrett DC, Kahraman SS, He Z, Wang LV. Numerical modeling of the multi-stage Stern-Gerlach experiment by Frisch and Segre using co-quantum dynamics via the Bloch equation. arXiv preprint arXiv:220813444. 2022.
48. He Z, Titimbo K, Garrett DC, Kahraman SS, Wang LV. Numerical modeling of the multi-stage Stern-Gerlach experiment by Frisch and Segre using co-quantum dynamics via the Schrodinger equation. arXiv preprint arXiv:220814588. 2022.
49. Bloch F. Nuclear Induction. Physical Review. 1946;70(7-8):460-74. doi: 10.1103/physrev.70.460.
50. Kahraman SS, Titimbo K, He Z, Shen J-T, Wang LV. Quantum mechanical modeling of the multi-stage Stern-Gerlach experiment by Frisch and Segre using the von Neumann equation. arXiv preprint arXiv:221011553. 2022.
51. Fuchs TM, Schäfer R. Double Stern-Gerlach experiments on Mn@ Sn 12: Refocusing of a paramagnetic superatom. Physical Review A. 2018;98(6):063411.
52. Einstein A. Remarks concerning the essays brought together in this co-operative volume. In: Schilpp PA, editor. Albert Einstein: Philosopher-Scientist. Library of Living Philosophers. La Salle: Open Court; 1949. p. 665-88.
53. Bjorken JD, Drell SD. Relativistic Quantum Mechanics. New York: Mcgraw-Hill College; 1964.
54. Gibbons JJ, Bartlett JH. The magnetic moment of the K^{39} nucleus. Physical Review. 1935;47(9):692-4. doi: 10.1103/physrev.47.692.
55. Hartree DR. Results of calculations of atomic wave functions. II.—Results for K^+ and Cs^+. Proceedings of the Royal Society of London Series A. 1934;143(850):506-17.
56. Wittig C. The Landau−Zener formula. J Phys Chem B. 2005;109(17):8428-30. doi: 10.1021/jp040627u.
57. Wilczek F. Majorana and condensed matter physics. In: Esposito S, editor. The Physics of Ettore Majorana: Theoretical, Mathematical, and Phenomenological. Cambridge University Press; 2014. p. 279-302.
58. Kofman PO, Ivakhnenko OV, Shevchenko SN, Nori F. Majorana's approach to nonadiabatic transitions validates the adiabatic-impulse approximation. arXiv preprint arXiv:220800481. 2022.
59. Lambropoulos P, Petrosyan D. Fundamentals of Quantum Optics and Quantum Information. Springer; 2007.
60. Bell JS. On the problem of hidden variables in quantum mechanics. Reviews of Modern Physics. 1966;38(3):447-52. doi: 10.1103/RevModPhys.38.447.
61. Shin DK, Henson BM, Hodgman SS, Wasak T, Chwedeńczuk J, Truscott AG. Bell correlations between spatially separated pairs of atoms. Nature Communications. 2019;10(1). doi: 10.1038/s41467-019-12192-8.
62. Thomas KF, Henson BM, Wang Y, Lewis-Swan RJ, Kheruntsyan KV, Hodgman SS, et al. A matter wave Rarity-Tapster interferometer to demonstrate non-locality. arXiv preprint arXiv:220608560. 2022.
63. Wang LV. Multi-stage Stern–Gerlach experiment modeled. Journal of Physics B: Atomic, Molecular and Optical Physics. 2023;56(10):105001. doi: 10.1088/1361-6455/acc149.

Supplementary Material

Multi-stage Stern–Gerlach experiment modeled

Lihong V. Wang*

Department of Electrical Engineering
Andrew and Peggy Cherng Department of Medical Engineering
California Institute of Technology
1200 E. California Blvd., MC 138-78, Pasadena, CA 91125, USA

* Correspondence to LVW@caltech.edu

ORCID: 0000-0001-9783-4383

Appendix 1. Derivation of torque-averaged fields

Given the focus of the Landau–Lifshitz–Gilbert equation on torque, we derive the torque-averaged magnetic flux densities applied on the electron and the nucleus by each other.

In relativistic quantum mechanics, the momentum density in the Dirac wave field is given by [33]

$$\vec{G} = \frac{\hbar}{2i}[\psi^\dagger \nabla\psi - (\nabla\psi^\dagger)\psi] + \frac{\hbar}{4}\nabla \times (\psi^\dagger \vec{\sigma}_{4\times4}\psi). \tag{31}$$

Here, ψ denotes the spatial wave function, ψ_s, multiplied by the spinor $w^1(0) = (1,0,0,0)^\dagger$; $\vec{\sigma}_{4\times4} = \sigma_1\hat{x} + \sigma_2\hat{y} + \sigma_3\hat{z}$, where $\sigma_1 = -i\alpha_2\alpha_3$, $\sigma_2 = -i\alpha_3\alpha_1$, $\sigma_3 = -i\alpha_1\alpha_2$; matrices α_1, α_2, and α_3 are from the Dirac equation [53]:

$$\alpha_1 = \begin{pmatrix} 0 & 0 & 0 & 1 \\ 0 & 0 & 1 & 0 \\ 0 & 1 & 0 & 0 \\ 1 & 0 & 0 & 0 \end{pmatrix}, \alpha_2 = \begin{pmatrix} 0 & 0 & 0 & -i \\ 0 & 0 & i & 0 \\ 0 & -i & 0 & 0 \\ i & 0 & 0 & 0 \end{pmatrix}, \text{and } \alpha_3 = \begin{pmatrix} 0 & 0 & 1 & 0 \\ 0 & 0 & 0 & -1 \\ 1 & 0 & 0 & 0 \\ 0 & -1 & 0 & 0 \end{pmatrix}. \tag{32}$$

While the first term on the right side of Eq. 31 is attributed to the translational motion of the electron, the second term is associated with circulating flow of energy [33].

Following Ohanian [33], an s orbital wave function is considered; $\psi_s^\dagger\psi_s$ is set to the Gaussian distribution,

$$\rho(r) = \left(\frac{1}{\pi a_0^2}\right)^{\frac{3}{2}} \exp\left(-\frac{r^2}{a_0^2}\right), \tag{33}$$

where r denotes the radial coordinate. The average radius, $\frac{2\,a_0}{\sqrt{\pi}}$, is set to the van der Waals atomic radius, R.

While the first term in Eq. 31 vanishes, the second term becomes

$$\vec{G} = \frac{\hbar}{2a_0^2}\rho\hat{z} \times \vec{r}. \tag{34}$$

The differential element of the magnetic dipole moment is [33]

$$d\vec{m}_e(\vec{r}) = \gamma_e\vec{r} \times \left(\frac{\hbar}{4}\nabla \times (\psi^\dagger\gamma^0\vec{\sigma}_{4\times4}\psi)\right) d^3\vec{r}. \tag{35}$$

From

$$\gamma^0 = \begin{pmatrix} 1 & 0 & 0 & 0 \\ 0 & 1 & 0 & 0 \\ 0 & 0 & -1 & 0 \\ 0 & 0 & 0 & -1 \end{pmatrix}, \tag{36}$$

we reach

$$d\vec{m}_e(\vec{r}) = \gamma_e\vec{r} \times \vec{G}d^3\vec{r}. \tag{37}$$

The field at location $\vec{r}$ from $\vec{\mu}_n$ is given by [31, 32]

$$\vec{B}(\vec{r}) = \frac{\mu_0}{4\pi r^3}[3(\vec{\mu}_n \cdot \hat{r})\hat{r} - \vec{\mu}_n] + \frac{2\mu_0}{3}\vec{\mu}_n \delta(\vec{r}). \tag{38}$$

The differential element of the torque from $\vec{\mu}_n$ is

$$d\vec{\tau}_n(\vec{r}) = d\vec{m}_e(\vec{r}) \times \vec{B}(\vec{r}). \tag{39}$$

Volumetric integration yields

$$\vec{m}_e(\vec{r}) = \int d\vec{m}_e = \gamma_e \frac{\hbar}{2}\hat{z}, \tag{40}$$

which equals $\vec{\mu}_e$, and

$$\vec{\tau}_n = \int d\vec{\tau}_n = \vec{\mu}_e \times \left(\frac{4\mu_0}{3\pi^3 R^3}\vec{\mu}_n\right). \tag{41}$$

Therefore, the torque-averaged B field from $\vec{\mu}_n$ applied on the electron is given by

$$\vec{B}_n = \frac{4\mu_0}{3\pi^3 R^3}\vec{\mu}_n. \tag{42}$$

Now, we switch to a classical approach. On the time scale pertinent to the precession cycle, we model the much faster motion of the s valence electron with the probability density, ρ.

The current density at position $\vec{r}$ is given by

$$\vec{j} = -e\rho\vec{\omega} \times \vec{r}, \tag{43}$$

where $-e$ denotes the electron charge and $\vec{\omega}$ denotes the angular velocity.

The differential element of the magnetic dipole moment is

$$d\vec{m}_e(\vec{r}) = \frac{1}{2}\vec{r} \times \vec{j} d^3\vec{r}. \tag{44}$$

The differential element of the torque is (Eq. 39)

$$d\vec{\tau}_n(\vec{r}) = d\vec{m}_e(\vec{r}) \times \vec{B}(\vec{r}). \tag{45}$$

Three distributions of ρ are considered.

First, ρ is set to the Gaussian distribution given by Eq. 33. Volumetric integration produces

$$\vec{m}_e = \int d\vec{m}_e = -\frac{1}{2}ea_0^2\vec{\omega} = -\frac{\pi}{8}eR^2\vec{\omega} \tag{46}$$

and

$$\vec{\tau}_n = \int d\vec{\tau}_n = \vec{m}_e \times \left(\frac{4\mu_0}{3\pi^3 R^3}\vec{\mu}_n\right). \tag{47}$$

Averaging yields

$$\langle\vec{\tau}_n\rangle = \langle\vec{m}_e\rangle \times \left(\frac{4\mu_0}{3\pi^3 R^3}\vec{\mu}_n\right). \tag{48}$$

For an s valence electron, both the orbital angular momentum and the orbital magnetic moment vanish; accordingly, we have $\langle\vec{m}_e\rangle = \vec{\mu}_e$, which is due to spin only. Consequently,

$$\langle \vec{\tau}_n \rangle = \vec{\mu}_e \times \left(\frac{4\mu_0}{3\pi^3 R^3} \vec{\mu}_n \right). \tag{49}$$

Therefore, we reach

$$\vec{B}_n = \frac{4\mu_0}{3\pi^3 R^3} \vec{\mu}_n, \tag{50}$$

which agrees with the relativistic quantum mechanical solution (Eq. 42).

Second, using the tabulated approximate 4*s* wave function, ψ_s, for potassium (Table S1) [54] based on Hartree's self-consistent field [55], we numerically reached

$$\vec{B}_n = \frac{0.138\mu_0}{\pi R^3} \vec{\mu}_n, \tag{51}$$

where the average radius is set to R. Coincidentally, this solution differs from the Gaussian solution (Eq. 50) by only 2%.

Table S1. Normalized $P(4s)$ for potassium. $\psi_s(0) = \sqrt{9.76/(4\pi)}$ and $\psi_s(r) = P/\left(\sqrt{4\pi a_0}r\right)$ for $r > 0$. [54]

r/a_0	P	r/a_0	P	r/a_0	P	r/a_0	P
0.000	0.0000	0.280	–0.0993	2.800	–0.2524	13.000	–0.0634
0.005	0.0142	0.300	–0.0972	3.000	–0.2926	14.000	–0.0443
0.010	0.0257	0.350	–0.0830	3.200	–0.3279	15.000	–0.0305
0.015	0.0349	0.400	–0.0598	3.400	–0.3583	16.000	–,0209
0.020	0.0421	0.450	–0.0312	3.600	–0.3840	17.000	–0.0138
0.030	0.0509	0.500	–0.0003	3.800	–0.4052	18.000	–0.0095
0.040	0.0540	0.550	0.0307	4.000	–0.4221	19.000	–0.0063
0.050	0.0527	0.600	0.0601	4.500	–0.4476	20.000	–0.0042
0.060	0.0480	0.700	0.1105	5.000	–0.4530	21.000	–0.0028
0.070	0.0409	0.800	0.1465	5.500	–0.4430	22.000	–0.0018
0.080	0.0321	0.900	0.1679	6.000	–0.4220	23.000	–0.0012
0.090	0.0220	1.000	0.1761	6.500	–0.3937	24.000	–0.0008
0.100	0.0113	1.100	0.1734	7.000	–0.3609	25.000	–0.0005
0.120	–0.0108	1.200	0.1623	7.500	–0.3264	26.000	–0.0003
0.140	–0.0321	1.400	0.1226	8.000	–0.2916	27.000	–0.0002
0.160	–0.0511	1.600	0.0699	8.500	–0.2578	28.000	–0.0001
0.180	–0.0673	1.800	0.0119	9.000	–0.2261	29.000	–0.0001
0.200	–0.0801	2.000	–0.0470	9.500	–0.1967	30.000	0.0000
0.220	–0.0896	2.200	–0.1040	10.000	–0.1700	31.000	0.0000
0.240	–0.0958	2.400	–0.1578	11.000	–0.1246		
0.260	–0.0989	2.600	–0.2074	12.000	–0.0896		

Third, ρ is set to the following top-hat distribution, which is a zeroth-order approximation to the actual distribution:

$$\rho(r) = \frac{3}{4\pi R^3} \tag{52}$$

for $r \leq R$ and $\rho = 0$ otherwise. Repeating the derivation starting from Eq. 43 yields

$$\vec{B}_n = \frac{5\mu_0}{16\pi R^3}\vec{\mu}_n. \tag{53}$$

In addition to the above torque-averaged fields, for comparison, the self-averaged fields from Eq. 38 are derived:

$$\vec{B}_n = \frac{2\mu_0}{3}\rho(0)\vec{\mu}_n. \tag{54}$$

For the Gaussian, tabulated, and top-hat distributions, $\rho(0) = \frac{8}{\pi^3 R^3}, \frac{14.2}{\pi R^3}$, and $\frac{3}{4\pi R^3}$, respectively; correspondingly, $\vec{B}_n = \frac{16\mu_0}{3\pi^3 R^3}\vec{\mu}_n, \frac{28.4\mu_0}{3\pi R^3}\vec{\mu}_n$, and $\frac{\mu_0}{2\pi R^3}\vec{\mu}_n$. These self-averaged fields, related to the Fermi contact interaction, are expected to be less compatible with the torque-based Landau–Lifshitz–Gilbert and CQD equations than the above torque-averaged fields.

The six solutions for $\vec{B}_n$ differ only by a constant factor. Eq. 53, however, predicts the experimental observation (Fig. 4) most accurately, achieving a coefficient of determination of $R^2 = 0.9787$. The alternatives produce negative R^2, indicating worse accuracy than modeling with a horizontal line intercepting at the mean observation. Therefore, we choose the torque-averaged field given by Eq. 53, rewritten below:

$$\vec{B}_n = \frac{5\mu_0}{16\pi R^3}\vec{\mu}_n. \tag{55}$$

Reciprocally, the torque-averaged field from $\vec{\mu}_e$ applied on the nucleus is

$$\vec{B}_e = \frac{5\mu_0}{16\pi R^3}\vec{\mu}_e. \tag{56}$$

Appendix 2. Derivation of CQD equations of motion

We apply the Landau–Lifshitz–Gilbert equation to both $\hat{\mu}_e$ and $\hat{\mu}_n$, yielding

$$\frac{d\hat{\mu}_e}{dt} = \gamma_e \hat{\mu}_e \times \left(\vec{B} + \vec{B}_n\right) - k_i \hat{\mu}_e \times \frac{d\hat{\mu}_e}{dt} \tag{57}$$

and

$$\frac{d\hat{\mu}_n}{dt} = \gamma_n \hat{\mu}_n \times \left(\vec{B} + \vec{B}_e\right) - k_i \hat{\mu}_n \times \frac{d\hat{\mu}_n}{dt}. \tag{58}$$

The external field is

$$\vec{B} = \begin{pmatrix} 0 \\ B_y \\ B_z \end{pmatrix}, \tag{59}$$

where B_x is neglected for brevity. The internal torque-averaged fields from the nucleus and the electron applied on each other (Appendix 1) are

$$\vec{B}_n = B_n \hat{\mu}_n \tag{60}$$

and

$$\vec{B}_e = B_e \hat{\mu}_e. \tag{61}$$

We have

$$\hat{\mu}_e = \begin{pmatrix} \sin\theta_e \cos\phi_e \\ \sin\theta_e \sin\phi_e \\ \cos\theta_e \end{pmatrix} \tag{62}$$

and

$$\hat{\mu}_n = \begin{pmatrix} \sin\theta_n \cos\phi_n \\ \sin\theta_n \sin\phi_n \\ \cos\theta_n \end{pmatrix}, \tag{63}$$

where θ and ϕ denote the polar and azimuthal angles, respectively.

Combining the above equations yields

$$\dot{\theta}_e = -\gamma_e\left[B_y \cos\phi_e + B_n \sin\theta_n \sin(\phi_n - \phi_e)\right] + k_i \dot{\phi}_e \sin\theta_e, \tag{64}$$

$$\dot{\theta}_n = -\gamma_n\left[B_y \cos\phi_n + B_e \sin\theta_e \sin(\phi_e - \phi_n)\right] + k_i \dot{\phi}_n \sin\theta_n, \tag{65}$$

$$\dot{\phi}_e = -\gamma_e\left\{B_z + B_n \cos\theta_n - \cot\theta_e \left[B_y \sin\phi_e + B_n \sin\theta_n \cos(\phi_n - \phi_e)\right]\right\} - \frac{k_i \dot{\theta}_e}{\sin\theta_e}, \tag{66}$$

and

$$\dot{\phi}_n = -\gamma_n\left\{B_z + B_e \cos\theta_e - \cot\theta_n \left[B_y \sin\phi_n + B_e \sin\theta_e \cos(\phi_e - \phi_n)\right]\right\} - \frac{k_i \dot{\theta}_n}{\sin\theta_n}. \tag{67}$$

To implement the second CQD postulate, we revise the sign of the last term in each of the above four equations, producing the CQD equations of motion (Eq. 5–8). Note that azimuthal angles are not defined when the polar angles are 0 or π. Therefore, when $\theta_e = 0$ or π, we use $\dot{\phi}_e = 0$; when $\theta_n = 0$ or π, we use $\dot{\phi}_n = 0$.

If $B_x \neq 0$, the above equations can be extended by the following substitutions:

$$B_y \cos\phi_e \to -B_x \sin\phi_e + B_y \cos\phi_e,$$

$$B_y \cos\phi_n \to -B_x \sin\phi_n + B_y \cos\phi_n,$$

$$B_y \sin\phi_e \to B_x \cos\phi_e + B_y \sin\phi_e,$$

and

$$B_y \sin\phi_n \to B_x \cos\phi_n + B_y \sin\phi_n.$$

Appendix 3. CQD derivation of density operator and wave function

CQD reproduces the quantum mechanical density operator and wave function with an isotropic angular distribution of co-quanta ($\hat{\mu}_n$) and extends them with an anisotropic angular distribution of co-quanta.

For a given $\hat{\mu}_e$, the CQD prediction expressions (see Methods) for two independent realizations are written in dual spaces [17]:

$$|\hat{\mu}_e © \hat{\mu}_{ni}\rangle = C_{i+}(\hat{\mu}_e, \hat{\mu}_{ni})|+z\rangle + C_{i-}(\hat{\mu}_e, \hat{\mu}_{ni})\exp(i\phi_e)|-z\rangle \tag{68}$$

and

$$\langle \hat{\mu}_e © \hat{\mu}_{nj}| = C_{j+}(\hat{\mu}_e, \hat{\mu}_{nj})\langle +z| + C_{j-}(\hat{\mu}_e, \hat{\mu}_{nj})\exp(-i\phi_e)\langle -z|. \tag{69}$$

Integer subscripts i and j denote independent realizations (i.e., $i \neq j$). Each binary coefficient represents either one or zero according to the branching condition (Eq. 10).

The pre-averaging density operator is defined as

$$\rho_0 \stackrel{\text{def}}{=} |\hat{\mu}_e © \hat{\mu}_{ni}\rangle\langle \hat{\mu}_e © \hat{\mu}_{nj}|, \tag{70}$$

which serves as a bridge to quantum mechanics [17]. Substitution of Eq. 68 and 69 results in

$$\rho_0 = [C_{i+}|+z\rangle + C_{i-}\exp(i\phi_e)|-z\rangle]\,[C_{j+}\langle +z| + C_{j-}\exp(-i\phi_e)\langle -z|]. \tag{71}$$

Expansion leads to

$$\rho_0 = C_{i+}C_{j+}|+z\rangle\langle +z| + C_{i-}C_{j-}|-z\rangle\langle -z|$$
$$+C_{i+}C_{j-}\exp(-i\phi_e)|+z\rangle\langle -z| + C_{i-}C_{j+}\exp(+i\phi_e)|-z\rangle\langle +z|. \tag{72}$$

If the dual vectors represented identical realizations, the cross terms would vanish because the binary coefficients are mutually exclusive for each realization: $C_{i\pm} \cdot C_{i\mp} = 0$ and $C_{j\pm} \cdot C_{j\mp} = 0$.

If $\hat{\mu}_n$ is random for a given $\hat{\mu}_e$, ensemble averaging ρ_0 over all realizations of $\hat{\mu}_n$, denoted by $\langle \quad \rangle_n$, yields

$$\rho_1 = \langle \rho_0 \rangle_n = \langle C_{i+}C_{j+}\rangle_n|+z\rangle\langle +z| + \langle C_{i-}C_{j-}\rangle_n|-z\rangle\langle -z|$$
$$+\langle C_{i+}C_{j-}\exp(-i\phi_e)\rangle_n|+z\rangle\langle -z| + \langle C_{i-}C_{j+}\exp(+i\phi_e)\rangle_n|-z\rangle\langle +z|. \tag{73}$$

The following equations are invoked next: $\langle C_{i+}\rangle_n = \langle C_{j+}\rangle_n$, denoted by $\langle C_+\rangle_n$; $\langle C_{i-}\rangle_n = \langle C_{j-}\rangle_n$, denoted by $\langle C_-\rangle_n$. Given the independence of the two realizations ($i \neq j$), we have $\langle C_{i\pm}C_{j\pm}\rangle_n = \langle C_{i\pm}\rangle_n\langle C_{j\pm}\rangle_n = \langle C_\pm\rangle_n^2$ and $\langle C_{i\pm}C_{j\mp}\rangle_n = \langle C_{i\pm}\rangle_n\langle C_{j\mp}\rangle_n = \langle C_+\rangle_n\langle C_-\rangle_n$, yielding

$$\rho_1 = \langle C_+\rangle_n^2|+z\rangle\langle +z| + \langle C_-\rangle_n^2|-z\rangle\langle -z|$$
$$+\langle C_+\rangle_n\langle C_-\rangle_n\exp(-i\phi_e)|+z\rangle\langle -z| + \langle C_-\rangle_n\langle C_+\rangle_n\exp(+i\phi_e)|-z\rangle\langle +z|. \tag{74}$$

Factorization yields

$$\rho_1 = [\langle C_+\rangle_n|+z\rangle + \langle C_-\rangle_n\exp(i\phi_e)|-z\rangle]\,[\langle C_+\rangle_n\langle +z| + \langle C_-\rangle_n\exp(-i\phi_e)\langle -z|]. \tag{75}$$

For a pure state, invoking $\rho_1 = |\hat{\mu}_e\rangle\langle\hat{\mu}_e|$ retrieves the following *ket* equation:

$$|\hat{\mu}_e\rangle = \langle C_+\rangle_n |+z\rangle + \langle C_-\rangle_n \exp(i\phi_e)\,|-z\rangle. \tag{76}$$

If $\hat{\mu}_n$ follows the isotropic p_{n0} (Eq. 15), the expected probabilities of collapse are computed from Eq. 74 as follows:

$$\langle +z|\rho_1|+z\rangle = \langle C_+\rangle_n^2 = \int_{\theta_e}^{\pi} p_{n0} 2\pi \sin\theta_n \, d\theta_n = \cos^2\frac{\theta_e}{2} \tag{77}$$

and

$$\langle -z|\rho_1|-z\rangle = \langle C_-\rangle_n^2 = \int_{0}^{\theta_e} p_{n0} 2\pi \sin\theta_n \, d\theta_n = \sin^2\frac{\theta_e}{2}. \tag{78}$$

The integration limits are based on the branching condition (Eq. 10). Because p_{n0} is isotropic (i.e., spherical), the two probabilities are proportional to the solid angles formed by the down and up sides of the cone shaped by the initial Bloch vector [15] ($\hat{\mu}_e$) precessing over one cycle (Fig. S1). Each solid angle determines the probability of having the co-quantum on the corresponding side of the cone. In other words, the above two equations represent the probabilities of having the co-quantum on the corresponding side of the cone.

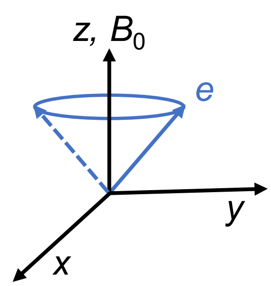

Fig. S1. Illustration of the cone of $\hat{\mu}_e$ formed by precession around the external main field, B_0, over the first Larmor cycle (i.e., before collapse). e: electron magnetic moment (principal quantum), $\hat{\mu}_e$. Any nuclear magnetic moment (co-quantum), $\hat{\mu}_n$, precessing around B_0 within the cone causes $\hat{\mu}_e$ to collapse down, whereas $\hat{\mu}_n$ precessing outside the cone causes $\hat{\mu}_e$ to collapse up. For a given polar angle θ_e of $\hat{\mu}_e$, the probability for the atom from the oven to reach the down branch in the first-stage Stern–Gerlach experiment is proportional to the solid angle of the cone because $\hat{\mu}_n$ follows an isotropic angular distribution. However, in subsequent-stage Stern–Gerlach experiments, the relation is revised because $\hat{\mu}_n$ follows an anisotropic angular distribution, such as the heart shape (Fig. 3, Inset a, solid line; Eq. 24).

Consequently, we reach the familiar quantum mechanical density operator,

$$\rho_1 = \cos^2\frac{\theta_e}{2}|+z\rangle\langle +z| + \sin^2\frac{\theta_e}{2}|-z\rangle\langle -z|$$
$$+\cos\frac{\theta_e}{2}\sin\frac{\theta_e}{2}\exp(-i\phi_e)\,|+z\rangle\langle -z| + \sin\frac{\theta_e}{2}\cos\frac{\theta_e}{2}\exp(+i\phi_e)\,|-z\rangle\langle +z|. \tag{79}$$

Factorization of the density operator yields

$$\rho_1 = \left[\cos\frac{\theta_e}{2}|+z\rangle + \sin\frac{\theta_e}{2}\exp(i\phi_e)\,|-z\rangle\right]\left[\cos\frac{\theta_e}{2}\langle +z| + \sin\frac{\theta_e}{2}\exp(-i\phi_e)\,\langle -z|\right]. \tag{80}$$

Invoking $\rho_1 = |\hat{\mu}_e\rangle\langle\hat{\mu}_e|$ for a pure state retrieves the following familiar quantum mechanical *ket* equation:

$$|\hat{\mu}_e\rangle = \cos\frac{\theta_e}{2}|+z\rangle + \sin\frac{\theta_e}{2}\exp(i\phi_e)\,|-z\rangle. \tag{81}$$

Therefore, CQD statistically reproduces the quantum mechanical wave function along with the probability amplitudes. As shown by Eq. 76, the moduli of probability amplitudes originate from averaging the binary coefficients in the CQD prediction expression.

If $\hat{\mu}_e$ is also random, further ensemble averaging ρ_1 over all realizations, denoted by $\langle\ \ \rangle_e$, yields

$$\rho_2 = \langle\rho_1\rangle_e = \langle\cos^2\frac{\theta_e}{2}\rangle_e\,|+z\rangle\langle+z| + \langle\sin^2\frac{\theta_e}{2}\rangle_e\,|-z\rangle\langle-z|$$
$$+\langle\cos\frac{\theta_e}{2}\sin\frac{\theta_e}{2}\exp(-i\phi_e)\rangle_e\,|+z\rangle\langle-z| + \langle\sin\frac{\theta_e}{2}\cos\frac{\theta_e}{2}\exp(+i\phi_e)\rangle_e\,|-z\rangle\langle+z|. \tag{82}$$

If $\hat{\mu}_e$ follows the isotropic p_{e0} (Eq. 19), the probabilities of collapse are computed as follows:

$$\langle+z|\rho_2|+z\rangle = \langle\cos^2\frac{\theta_e}{2}\rangle_e = \int_0^\pi\left[\cos^2\frac{\theta_e}{2}\right]p_{e0}2\pi\sin\theta_e\,d\theta_e = \frac{1}{2} \tag{83}$$

and

$$\langle-z|\rho_2|-z\rangle = \langle\sin^2\frac{\theta_e}{2}\rangle_e = \int_0^\pi\left[\sin^2\frac{\theta_e}{2}\right]p_{e0}2\pi\sin\theta_e\,d\theta_e = \frac{1}{2}. \tag{84}$$

The cross terms vanish due to the azimuthal integration of $\exp(-i\phi_e)$ over a full cycle of $\hat{\mu}_e$:

$$\langle+z|\rho_2|-z\rangle = \langle\cos\frac{\theta_e}{2}\sin\frac{\theta_e}{2}\exp(-i\phi_e)\rangle_e$$
$$= \int_0^\pi\cos\frac{\theta_e}{2}\sin\frac{\theta_e}{2}\left[\int_0^{2\pi}\exp(-i\phi_e)\,p_{e0}d\phi_e\right]\sin\theta_e\,d\theta_e = 0 \tag{85}$$

and

$$\langle+z|\rho_2|-z\rangle = \langle\sin\frac{\theta_e}{2}\cos\frac{\theta_e}{2}\exp(+i\phi_e)\rangle_e$$
$$= \int_0^\pi\sin\frac{\theta_e}{2}\cos\frac{\theta_e}{2}\left[\int_0^{2\pi}\exp(+i\phi_e)\,p_{e0}d\phi_e\right]\sin\theta_e\,d\theta_e = 0. \tag{86}$$

Therefore, we reach

$$\rho_2 = \frac{1}{2}|+z\rangle\langle+z| + \frac{1}{2}|-z\rangle\langle-z|. \tag{87}$$

This familiar quantum mechanical density operator represents the mixed state and cannot be factorized into a product of two pure-state wave functions.

If $\hat{\mu}_n$ follows the heart-shaped p_{n1} (Eq. 24), the probabilities of collapse become

$$\langle+z|\rho_1|+z\rangle = \langle C_+\rangle_n^2 = \int_{\theta_e}^\pi p_{n1}2\pi\sin\theta_n\,d\theta_n = 1-\sin^4\frac{\theta_e}{2} \tag{88}$$

instead of Eq. 77 and

$$\langle -z|\rho_1|-z\rangle = \langle C_-\rangle_n^2 = \int_0^{\theta_e} p_{n1} 2\pi \sin\theta_n \, d\theta_n = \sin^4\frac{\theta_e}{2} \tag{89}$$

instead of Eq. 78. Because p_{n1} is anisotropic (i.e., heart-shaped), the two probabilities are no longer simply proportional to the solid angles. However, the above two equations still represent the probabilities of having the co-quantum on the corresponding side of the cone (Fig. S1).

Accordingly, the wave function becomes

$$|\hat{\mu}_e\rangle = \sqrt{1 - \sin^4\frac{\theta_e}{2}}\,|+z\rangle + \sin^2\frac{\theta_e}{2}\exp(i\phi_e)\,|-z\rangle \tag{90}$$

instead of Eq. 81.

Appendix 4. Derivation of Majorana formula

The Majorana formula [10] or its Landau–Zener variant [12-14] was derived most intuitively in 2005 by Wittig [56]. Recent rederivations of the Majorana formula can be found in Wilczek [57] and Kofman [58]. Majorana stated that both the classical and the quantum-mechanical treatments require integration of the same differential equations [10, 11]. For completeness here, we follow Majorana's variable transformations and then abridge Wittig's solution but with a slightly altered contour integration.

For the inner rotation chamber (Fig. 3, IR), the B field along the y axis is approximated using a magnetic quadrupole (Fig. S2) [10, 11]:

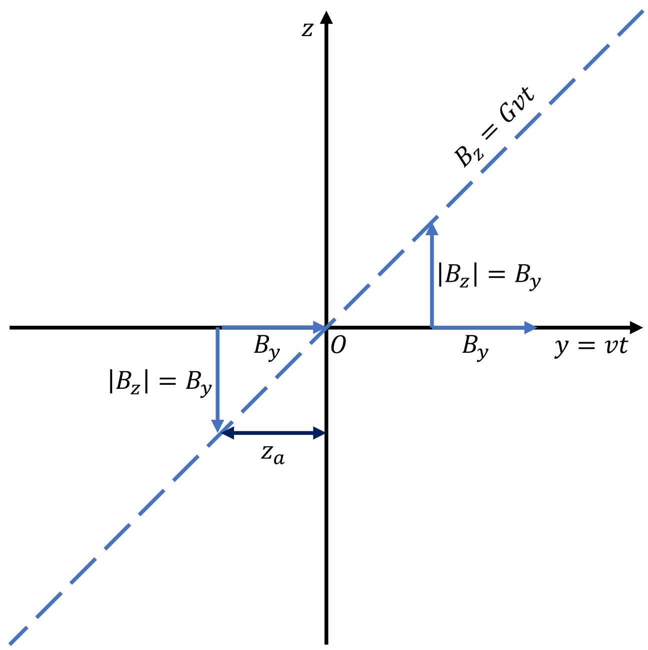

Fig. S2. Illustration of the magnetic field versus the y location of the atom in the inner rotation chamber (i.e., the middle stage). y denotes the axis of the atomic beam. Here, $B_y > 0$, and $G = \partial B_z/\partial y > 0$. For a given current, B_y is invariant with y while B_z is proportional to y (i.e., negative for $y < 0$, zero at $y = 0$, and positive for $y > 0$). At $y = \pm z_a$, we have $B_z = \pm B_y$ or $|B_z| = B_y$.

$$B_x = 0, \tag{91}$$

$$B_y = Gz_a, \tag{92}$$

and

$$B_z = Gvt. \tag{93}$$

Here, G is the derivative of B_z with respect to y (i.e., the gradient magnitude of B_z, $\partial B_z/\partial y$), z_a (1.05×10^{-4} m) is the vertical distance of the atomic beam from the center of the wire, v (800 m s^{-1}) is the most likely speed of atoms, and t is time set to zero at the null point of B_z. G is given by

$$G = \frac{\partial B_z}{\partial y} = \frac{2\pi}{\mu_0 I} B_r^2. \tag{94}$$

Here, I denotes the current carried by the wire along the $-x$ axis, and B_r (0.42×10^{-4} T) denotes the uniformly distributed remnant (residual) fringe magnetic flux density, which is parallel with the $+z$ axis. The magnetic field generated by the wire cancels the remnant field at the null point (NP) to produce an approximate quadrupole (Fig. 3, Inset b). For a given current, B_y is constant while B_z varies linearly with distance from the point where $B_z = 0$.

Majorana neglected the nuclear magnetic moment and induction. The Bloch equation leads to

$$\dot{\theta}_e = -\gamma_e B_y \cos\phi_e \tag{95}$$

and

$$\dot{\phi}_e = -\gamma_e\left[B_z - \cot\theta_e\, B_y \sin\phi_e\right], \tag{96}$$

which agree with Eq. 5 and 7 for $B_n = 0$ and $k_i = 0$.

Majorana transformed the polar and azimuthal angles into probability amplitudes then solved the transformed equations [10, 11]. We let

$$|\hat{\mu}\rangle = \begin{pmatrix} C_1 \\ C_2 \end{pmatrix}. \tag{97}$$

The Schrödinger equation becomes

$$i\hbar \frac{d}{dt}\begin{pmatrix} C_1 \\ C_2 \end{pmatrix} = H\begin{pmatrix} C_1 \\ C_2 \end{pmatrix}. \tag{98}$$

The Hamiltonian is

$$H = -\frac{1}{2}\hbar\gamma_e \vec{B} \cdot \vec{\sigma}. \tag{99}$$

Substituting the Pauli matrices $\vec{\sigma}$ yields

$$H = -\frac{1}{2}\hbar\gamma_e\left[B_x\begin{pmatrix} 0 & 1 \\ 1 & 0 \end{pmatrix} + B_y\begin{pmatrix} 0 & -i \\ i & 0 \end{pmatrix} + B_z\begin{pmatrix} 1 & 0 \\ 0 & -1 \end{pmatrix}\right]. \tag{100}$$

Merging terms gives

$$H = -\frac{1}{2}\hbar\gamma_e\begin{pmatrix} B_z & B_x - iB_y \\ B_x + iB_y & -B_z \end{pmatrix}. \tag{101}$$

Majorana defined the following dimensionless variables for time and adiabaticity, respectively [10, 11]:

$$\tau = \frac{1}{2}\sqrt{|\gamma_e G v|} \cdot t \tag{102}$$

and

$$k_m = \frac{|\gamma_e| B_y}{Gv/B_y} = \frac{|\gamma_e| B_y^2}{Gv} = \frac{z_a}{v}|\gamma_e| B_y. \tag{103}$$

The numerator, $|\gamma_e| B_y$, in the first fraction above represents the Larmor frequency about the y axis, whereas the denominator, Gv/B_y, represents approximately the rotation frequency of the field.

Accordingly, the Schrödinger equation is simplified to

$$\frac{d}{d\tau}\begin{pmatrix} c_1 \\ c_2 \end{pmatrix} = -i\begin{pmatrix} 2\tau c_1 - i\sqrt{k_m}c_2 \\ i\sqrt{k_m}c_1 - 2\tau c_2 \end{pmatrix}. \tag{104}$$

Majorana defined the following transformation of variables [10, 11], which is analogous to heterodyne detection with a chirped local oscillator to remove high-frequency signals:

$$\begin{pmatrix} c_1 \\ c_2 \end{pmatrix} = \begin{pmatrix} \exp(-i\tau^2)\, f \\ \exp(+i\tau^2)\, g \end{pmatrix}. \tag{105}$$

The Schrödinger equation becomes

$$\frac{d}{d\tau}\begin{pmatrix} f \\ g \end{pmatrix} = \sqrt{k_m}\begin{pmatrix} -\exp(+2i\tau^2)\, g \\ +\exp(-2i\tau^2)\, f \end{pmatrix}. \tag{106}$$

Eliminating variables yields

$$\left(\frac{d^2}{d\tau^2} \mp 4i\tau\frac{d}{d\tau} + k_m\right)\begin{pmatrix} f \\ g \end{pmatrix} = 0. \tag{107}$$

For $|f(-\infty)| = 1$, we solve for $|f(+\infty)|$. Following Wittig [56], we rewrite the equation for f as

$$4i\frac{df}{f} = \frac{d\tau}{\tau}\left(\frac{d^2 f}{d\tau^2}\frac{1}{f} + k_m\right). \tag{108}$$

Integrating over the entire flight yields

$$4i\int_{-\infty}^{+\infty}\frac{df}{f} = \int_{-\infty}^{+\infty}\frac{d\tau}{\tau}\left(\frac{d^2 f}{d\tau^2}\frac{1}{f} + k_m\right). \tag{109}$$

We select a positively oriented and indented contour that excludes the singularity at $\tau = 0$ in the complex plane (Fig. S3), whereas the opposite orientation would yield an unphysical outcome. Consequently, we have

$$4i\ln\frac{f(+\infty)}{f(-\infty)} = \oint \quad - \lim_{\varepsilon\to 0}\int_{\text{arc}} \quad - \lim_{R\to\infty}\int_{\text{Arc}}\frac{d\tau}{\tau}\left(\frac{d^2 f}{d\tau^2}\frac{1}{f} + k_m\right). \tag{110}$$

Here, ε is the radius of the small indenting semicircular arc, R is the radius of the large semicircular arc, and τ is now made complex without substitution to a new complex variable (because the typically adopted z is used already for space). Because no pole is inside the contour, the first integral on the right side vanishes.

At $\tau = 0$, Eq. 107 gives the residue,

$$\text{Res}_0 = \left(\frac{d^2 f}{d\tau^2}\frac{1}{f} + k_m\right)\Big|_{\tau=0} = 0. \tag{111}$$

Thus, the second integral along the small arc on the right side of Eq. 110 vanishes too.

As $\tau \to \infty$, $\frac{d^2 f}{d\tau^2}\frac{1}{f} \to 0$ [56]; substitution into the third integral along the large arc yields

$$4i \ln \frac{f(+\infty)}{f(-\infty)} = -k_m \lim_{R\to\infty} \int_{\mathrm{Arc}} \frac{d\tau}{\tau}. \tag{112}$$

Letting $\tau = R\exp(i\beta)$ leads to

$$\ln \frac{f(+\infty)}{f(-\infty)} = -\frac{k_m}{4i} \lim_{R\to\infty} \int_0^{\pi} \frac{R\exp(i\beta) i d\beta}{R\exp(i\beta)} = -\frac{\pi k_m}{4}. \tag{113}$$

Therefore,

$$\frac{|f(+\infty)|}{|f(-\infty)|} = \exp\left(-\frac{\pi k_m}{4}\right). \tag{114}$$

Substituting $|f(-\infty)| = 1$, we reach

$$|f(+\infty)| = \exp\left(-\frac{\pi k_m}{4}\right). \tag{115}$$

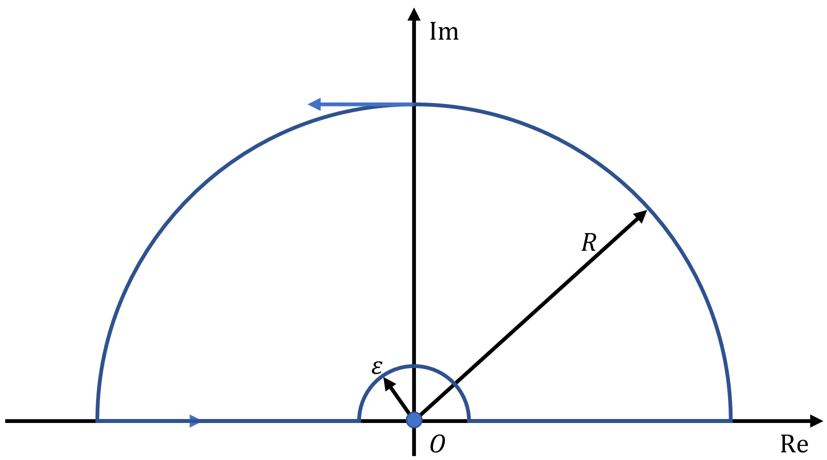

Fig. S3. Contour on the complex plane of τ for the integration. The solid circle indicates the pole at $\tau = 0$. Adapted from Wittig [56].

Majorana [10, 11] reasoned that because B_z reverses its orientation along the flight path, the probability of spin flip, W_m, is given by $|f(+\infty)|^2$ instead of $|g(+\infty)|^2$. The further justification that we found is the initial adiabatic flip induced when the atom passes above the wire [47]. Therefore, we obtain

$$W_m = \exp\left(-\frac{\pi k_m}{2}\right). \tag{116}$$

Here, $k_m > 0$. If $k_m < 0$, one may extend the solution to $\exp\left(-\frac{\pi|k_m|}{2}\right)$. Substitution of Eq. 103 results in

$$W_m = \exp\left(-\frac{\pi z_a}{2v}|\gamma_e|B_y\right). \tag{117}$$

Appendix 5. Derivation of CQD formula

We derive the CQD formula for the probability of spin flip in the inner rotation chamber (Fig. 3, IR) in the presence of both the quadrupole field and the nuclear magnetic moment.

The average polar angle of $\vec{B}_n$, $\langle\theta_n\rangle$, is derived from the heart shape given by Eq. 24:

$$\langle\theta_n\rangle = \int_0^{\pi} \theta_n p_{n1} 2\pi \sin\theta_n \, d\theta_n = 5\pi/8. \tag{118}$$

To reach an approximate analytical solution, we hold θ_n at $\langle\theta_n\rangle$ as a representative value throughout the inner rotation chamber.

The presence of $\vec{B}_n$ alters both the remnant field due to the projection of $\vec{B}_n$ to the z axis, given by $B_n \cos\langle\theta_n\rangle$, and the transverse field due to the transverse projection of $\vec{B}_n$, represented by $B_n \sin\langle\theta_n\rangle \exp(i\phi_n)$. To extend the Majorana solution presented in Appendix 4, we first substitute the remnant field as follows:

$$B_r \to B_r' = B_r + B_n \cos\langle\theta_n\rangle. \tag{119}$$

Accordingly, we update the field gradient:

$$G = \frac{2\pi}{\mu_0 I} {B_r}^2 \to G' = \frac{2\pi}{\mu_0 I} {B_r'}^2. \tag{120}$$

The quadrupole field along the y axis is still given by the same equations but with the corrected field gradient:[10, 11]

$$B_x' = 0, \tag{121}$$

$$B_y' = G' z_a, \tag{122}$$

and

$$B_z' = G' v t. \tag{123}$$

Following Majorana [10, 11], we define the dimensionless time as

$$\tau = \frac{1}{2}\sqrt{|\gamma_e G' v|} \cdot t \tag{124}$$

and the dimensionless adiabaticity parameter due to B_y' as

$$k_0 = \frac{|\gamma_e| B_y'}{G' v / B_y'} = \frac{z_a}{v} |\gamma_e| B_y'. \tag{125}$$

The numerator, $|\gamma_e| B_y'$, in the first fraction above represents the Larmor frequency about the y axis, whereas the denominator, $G' v / B_y'$, represents approximately the rotation frequency of the field. We similarly define the adiabaticity parameter due to the transverse field $B_n \sin\langle\theta_n\rangle$ as

$$k_1 = \frac{|\gamma_e| (B_n \sin\langle\theta_n\rangle)}{G' v / (B_n \sin\langle\theta_n\rangle)} = \frac{z_a}{v} |\gamma_e| \frac{(B_n \sin\langle\theta_n\rangle)^2}{B_y'}. \tag{126}$$

We also compute the dimensionless counterpart of the Larmor frequency ω_n as

$$w_n = \frac{d\phi_n}{d\tau} = \frac{d\phi_n}{dt}\frac{dt}{d\tau} = \frac{2}{\sqrt{|\gamma_e G' v|}} \omega_n, \tag{127}$$

where $\omega_n = d\phi_n/dt$ was invoked.

Then, we substitute the total transverse field for the Schrödinger equation:

$$B_x \to B_x' + B_n \sin\langle\theta_n\rangle \cos\phi_n \tag{128}$$

and

$$B_y \to B_y' + B_n \sin\langle\theta_n\rangle \sin\phi_n. \tag{129}$$

Following the procedure presented in Appendix 4, we revise the Schrödinger equation to

$$\frac{d}{d\tau}\begin{pmatrix} c_1 \\ c_2 \end{pmatrix} = -i\begin{pmatrix} 2\tau & \sqrt{k_1}\exp(-i\phi_n) - i\sqrt{k_0} \\ \sqrt{k_1}\exp(i\phi_n) + i\sqrt{k_0} & -2\tau \end{pmatrix}\begin{pmatrix} c_1 \\ c_2 \end{pmatrix}. \tag{130}$$

Defining

$$\begin{pmatrix} c_1 \\ c_2 \end{pmatrix} = \begin{pmatrix} \exp(-i\tau^2)\, f(\tau) \\ \exp(+i\tau^2)\, g(\tau) \end{pmatrix}, \tag{131}$$

we reach

$$\frac{d}{d\tau}\begin{pmatrix} f(\tau) \\ g(\tau) \end{pmatrix} = \begin{pmatrix} \left[-i\sqrt{k_1}\exp(-i\phi_n) - \sqrt{k_0}\right]\exp(+2i\tau^2)\, g(\tau) \\ \left[-i\sqrt{k_1}\exp i\phi_n + \sqrt{k_0}\right]\exp(-2i\tau^2)\, f(\tau) \end{pmatrix}. \tag{132}$$

Eliminating g yields

$$4i\frac{df}{f} = \frac{d\tau}{\tau - \frac{\sqrt{k_1}w_n}{4\left[\sqrt{k_1} - i\sqrt{k_0}\exp(i\phi_n)\right]}}\left\{\frac{d^2 f}{d\tau^2}\frac{1}{f} + \left[k_0 + k_1 + 2\sqrt{k_0 k_1}\sin(\phi_n)\right]\right\}. \tag{133}$$

In the limiting case that $k_0 \gg k_1$, i.e., the extremely low-current region, we set $k_1 = 0$, reducing Eq. 133 to

$$4i\frac{df}{f} = \frac{d\tau}{\tau}\left\{\frac{d^2 f}{d\tau^2}\frac{1}{f} + k_0\right\}, \tag{134}$$

which is the same as Eq. 108. The solution with $|f(-\infty)| = 1$ is given by Eq. 115:

$$|f(+\infty)| = \exp\left(-\frac{\pi k_0}{4}\right). \tag{135}$$

From Eq. 25 in Results, the fraction of flip is given by $|f(+\infty)|^4$ instead of $|f(+\infty)|^2$ due to the heart-shaped p_{n1}:

$$W_2 = \exp(-\pi k_0) = \exp\left(-\pi\frac{z_a}{v}|\gamma_e|B_y'\right). \tag{136}$$

W_2 is shown in Fig. S4 below and Fig. 4. Because the pole in Eq. 134 is at $\tau = 0$, we call this effect null-point rotation.

Conversely, if we set $k_0 = 0$, Eq. 133 reduces to

$$4i\frac{df}{f} = \frac{d\tau}{\tau - \frac{w_n}{4}}\left\{\frac{d^2 f}{d\tau^2}\frac{1}{f} + k_1\right\}, \tag{137}$$

which resembles Eq. 108, however, with the pole shifted from 0 to $w_n/4$. The solution is likewise obtained as

$$|f(+\infty)| = \exp\left(-\frac{\pi k_1}{4}\right). \tag{138}$$

Similarly, the fraction of flip is

$$W_R = \exp(-\pi k_1), \tag{139}$$

which is shown in Fig. S4. The pole $\tau = w_n/4$ is converted using Eq. 124 and Eq. 127 to dimensional quantities as $\omega_{ez}(t) = \omega_n(t)$, where ω_{ez} denotes the Larmor frequency of $\vec{\mu}_e$ about the z axis and ω_n denotes the Larmor frequency of $\vec{\mu}_n$. Therefore, the flip is due to precession resonance between the magnetic moments of the nucleus and the electron, which we refer to as nuclear-resonant rotation.

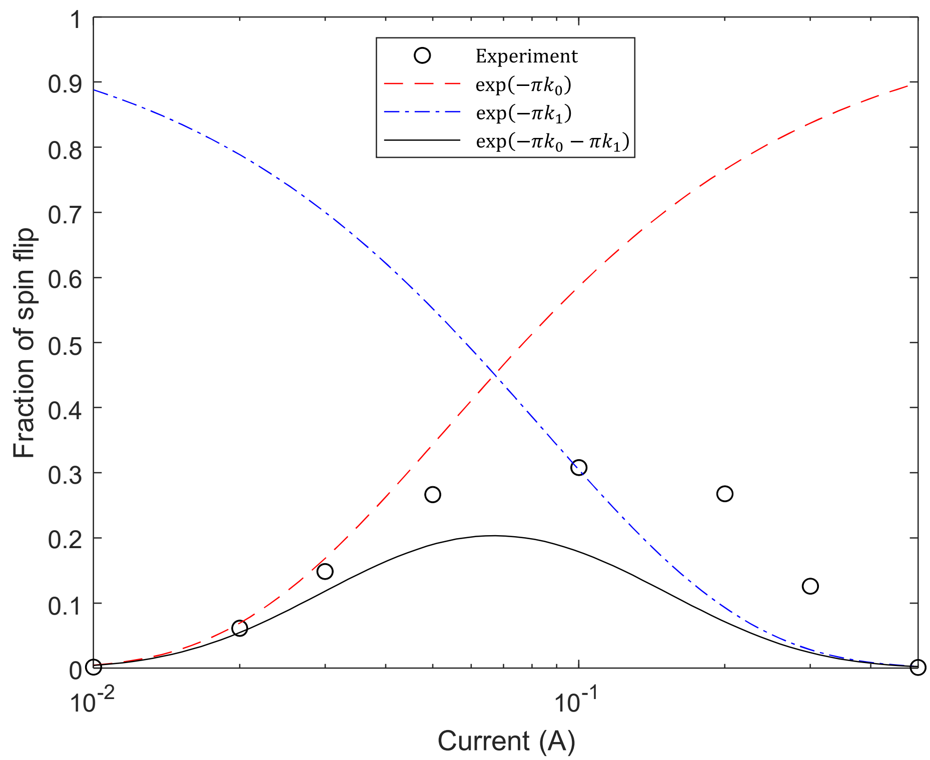

Fig. S4. Fraction of spin flip versus wire current. As the current increases from 0.01 A to 0.5 A, k_0 decreases inversely proportionally with the current from 1.701 to 0.034, and k_1 increases proportionally with the current from 0.038 to 1.891. When $B_y' = B_n \sin\langle\theta_n\rangle = 0.11 \times 10^{-4}$ T, $k_0 = k_1$; the corresponding current equals 0.067 A, about which the dashed and dash-dotted curves are mirror symmetric on the semilog plot. Experiment: Frisch–Segrè experiment.

There are three terms inside the square brackets in Eq. 133: $k_0 + k_1 + 2\sqrt{k_0 k_1}\sin(\phi_n)$. A direct combination of the first two terms yields the solid-line curve in Fig. S4, which predicts the fraction of flip accurately at the two ends but only qualitatively in the intermediate region. Below, we combine the terms more quantitatively. For an ensemble of atoms, the nuclear magnetic moment of each atom is given a random initial phase, ϕ_{n0}, at $t = 0$.

Given Eq. 25 in Results, we extend the Majorana solution (see Appendix 4) to

$$W_{\text{cqd}} = \sin^4\left(\frac{\alpha_r}{2}\right) = \exp(-E_{r0} - E_{r1} - E_i), \tag{140}$$

where α_r represents the polar rotation by the inner rotation chamber from the initial $\theta_e = 0$ and E_{r0}, E_{r1}, E_i represent contributions from null-point rotation, nuclear-resonant rotation, and induction, respectively. The fourth power is due to the heart-shaped p_{n1}.

The null-point rotation exponent is determined by the quadrature-summed (or the root-mean-squared) B field on the xy plane:

$$E_{r0} = \frac{\pi z_a}{v}|\gamma_e|\sqrt{B_y'^2 + (B_n \sin\langle\theta_n\rangle)^2}. \tag{141}$$

The quadrature sum can be derived through $\langle\left|iB_y' + B_n \sin\langle\theta_n\rangle \exp(i\phi_{n0})\right|^2\rangle^{1/2}$, where the ensemble average is over a uniform distribution of ϕ_{n0} and $B_n \sin\langle\theta_n\rangle \exp(i\phi_{n0})$ is the transverse component of $\vec{B}_n$ at the null point. One may consider $\pi\, B_y'/G'$, yielding πz_a (Eq. 122), as the effective flight path-length for the null-point rotation, πy_{r0} (Fig. S5). Here, $\pi y_{r0} = \pi z_a = \pi \times 0.105 \times 10^{-3} = 0.33 \times 10^{-3}$ m, which is a constant independent of the wire current. If $B_n = 0$, the quadrature sum reduces to B_y' as expected. E_{r0} is responsible for Curve 3 in Fig. 4, which predicts the experimental observation in the low-current region accurately. Further description can be found above Eq. 28.

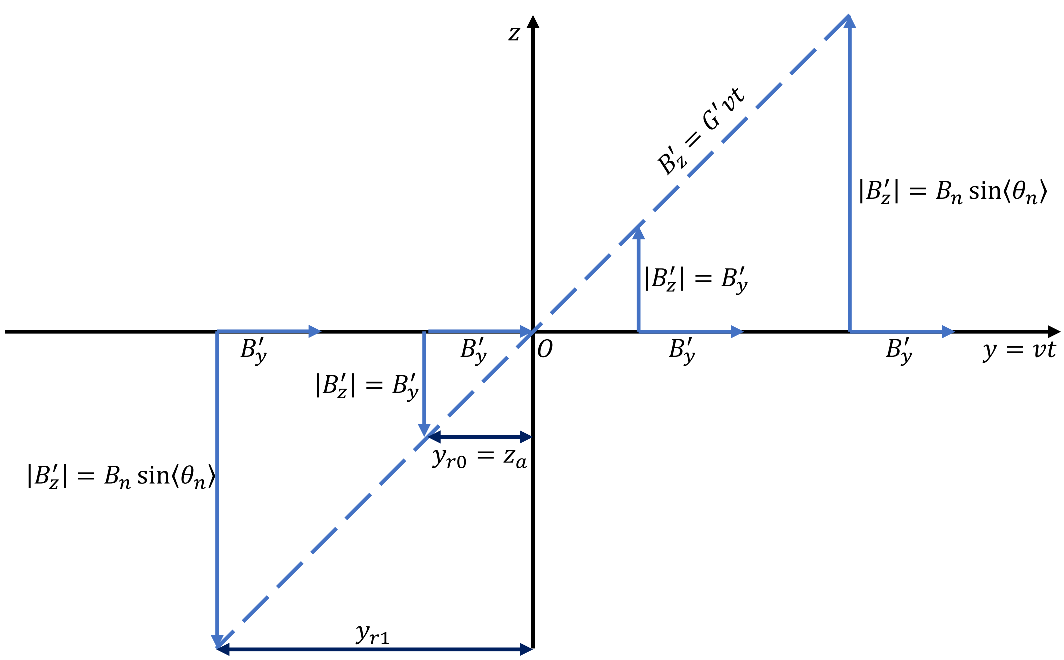

Fig. S5. Illustration of the magnetic field versus the y location of the atom in the inner rotation chamber (i.e., the middle stage). Here, $y_{r1}/y_{r0} = 3$, for the current of 0.2 A. For a given current, B_y' is invariant with y while B_z' is proportional to y (i.e., negative for $y < 0$, zero at $y = 0$, and positive for $y > 0$). $B_n \sin\langle\theta_n\rangle$ is the transverse projection of $\vec{B}_n$ on the xy plane. $G' = \partial B_z'/\partial y$.

At high currents where $I \geq 0.067$ A, B_y' becomes less than $B_n \sin\langle\theta_n\rangle$, and $k_1 \geq k_0$; consequently, nuclear-resonant rotation due to the rotating transverse component of $\vec{B}_n$ becomes substantial. The resonant-rotation exponent is approximated heuristically as

$$E_{r1} = \frac{1}{2}\left[\frac{\pi y_{r1}}{v}|\gamma_e|B_n \sin\langle\theta_n\rangle\right]^2 \left\{\frac{\pi y_{r1}}{v}\frac{1}{T_n}\right\}. \tag{142}$$

The term in the square bracket is analogous to the right-hand side of Eq. 141. This estimation is inspired by the following approximation for small fluctuations of a random variable X:

$$\langle\exp(X - \bar{X})\rangle \approx \exp\left(\frac{1}{2}\langle(X - \bar{X})^2\rangle\right) = \exp\left(\frac{1}{2}\mathrm{Var}[X]\right), \tag{143}$$

where Var denotes variance.

In analogy to $\pi y_{r0} = \pi\, B_y'/G'$ defined below Eq. 141, the effective flight path-length for nuclear-resonant rotation, πy_{r1}, is defined as (Fig. S5)

$$\pi y_{r1} = \frac{\pi B_n \sin\langle\theta_n\rangle}{G'} = \frac{\pi z_a B_n \sin\langle\theta_n\rangle}{B_y'}. \tag{144}$$

Because B_e is far greater than the field in the inner rotation chamber, the Larmor period of the nuclear magnetic moment is approximated to be

$$T_n = \frac{2\pi}{\gamma_n B_e}. \tag{145}$$

The curly bracket term in Eq. 142 represents the fraction of the Larmor period of the nuclear magnetic moment, denoted by f_{r1}, precessed during the flight time over πy_{r1}:

$$f_{r1} = \frac{\pi y_{r1}}{v T_n}. \tag{146}$$

One may consider $\pi y_{r1}/v$ as the effective nuclear-resonant time. Note that f_{r1} increases proportionally with the wire current. When f_{r1} approaches zero, the transverse component of $\vec{B}_n$ has no time to rotate or vary within the effective flight path-length for nuclear-resonant rotation; thus, its variance vanishes. Conversely, when f_{r1} approaches unity, the mean transverse component of $\vec{B}_n$ nears zero; thus, the variance peaks towards $(B_n \sin\langle\theta_n\rangle)^2$. In between, the variance is approximated by linear interpolation.

We have $\pi y_{r1}/(\pi y_{r0}) = B_n \sin\langle\theta_n\rangle/B_y'$. At the current of 0.067 A that divides the two regimes of current, $\pi y_{r1} = \pi y_{r0} = 0.33 \times 10^{-3}$ m, yielding $\pi y_{r1}/(\pi y_{r0}) = 1$. As illustrated in Fig. S5, at the current of 0.2 A, πy_{r1} equals 0.98×10^{-3} m, yielding $\pi y_{r1}/(\pi y_{r0}) = 3.0$. At the maximum current of 0.5 A, πy_{r1} increases to 2.5×10^{-3} m, yielding $\pi y_{r1}/(\pi y_{r0}) = 7.5$; f_{r1} reaches 0.34. In comparison, the counterpart f_{r0} during the flight time over πy_{r0} is only $0.34 \times \pi y_{r0}/(\pi y_{r1}) = 0.045 \ll 1$; thus, the transverse field is stable, i.e., its angular variation is much less than 2π. Therefore, the null-point rotation is due to the static and quasi-static transverse field within πy_{r0}, whereas the nuclear-resonant rotation is due to the rotating transverse field within πy_{r1}. Disrupted by the null-point rotation in combination with the random ϕ_{n0} in the ensemble of atoms (see Eq. 133), the nuclear-resonant rotation contributes to the fraction of flip through the variance (instead of Eq. 139 in the absence of the null-point rotation). Note that one may consider the null-point rotation as a resonant effect but at a zero Larmor frequency.

Combining terms yields

$$E_{r1} = \frac{\pi^2|\gamma_e|^2\gamma_n z_a^3}{4v^3}\frac{B_e(B_n \sin\langle\theta_n\rangle)^5}{B_y'^3}. \tag{147}$$

Expressing B_y' in terms of the current, I, using Eq. 120 and 122 gives

$$E_{r1} = \frac{\mu_0^3|\gamma_e|^2\gamma_n}{32\pi v^3}\frac{B_e(B_n \sin\langle\theta_n\rangle)^5}{(B_r+B_n \cos\langle\theta_n\rangle)^6}I^3. \tag{148}$$

Using the dimensionless adiabaticity parameters k_0 (Eq. 125) and k_1 (Eq. 126), we simplify Eq. 141 and 142 to

$$E_{r0} = \pi k_0\sqrt{1 + k_1/k_0} = \pi\sqrt{k_0^2 + k_0 k_1} \tag{149}$$

and

$$E_{r1} = \frac{1}{2}[\pi k_1\ ]^2\{f_{r1}\}. \tag{150}$$

Thus, E_{r0} is due to the quadrature sum of k_0 and $\sqrt{k_0 k_1}$, and E_{r1} is due to k_1. Eq. 146 can be rewritten as $f_{r1} = \frac{\pi z_a}{vT_n}\sqrt{k_1/k_0}$. Substitution of the above two equations into Eq. 140 with $E_i = 0$ yields the fraction of flip

$$W_4 = \exp\left(-\pi\sqrt{k_0^2 + k_0 k_1} - \frac{1}{2}[\pi k_1\ ]^2 f_{r1}\right), \tag{151}$$

which produces Curve 4 in Fig. 4. If $f_{r1} = 0$, W_4 reduces to

$$W_3 = \exp\left(-\pi\sqrt{k_0^2 + k_0 k_1}\right), \tag{152}$$

which produces Curve 3 in Fig. 4. If $k_1 = 0$, W_3 reduces to

$$W_2 = \exp(-\pi k_0), \tag{153}$$

which produces Curve 2 in Fig. 4. If k_0 is computed without including the correction to the remnant field (Eq. 119), k_0 reduces to k_m; thus, W_2 reduces to

$$W_1 = \exp(-\pi k_m), \tag{154}$$

which produces Curve 1 in Fig. 4. Taking the square root of W_1 leads to

$$W_m = \exp(-\pi k_m/2), \tag{155}$$

which produces Curve m in Fig. 4.

The induction exponent is estimated as

$$E_i = 4k_i \int_{-T_f/2}^{+T_f/2}\left|\dot{\phi}_e\right| dt, \tag{156}$$

where T_f denotes the entire flight time corresponding to a path-length of 16.3 mm in the inner rotation chamber. The field generated from the wire contributes to induction. At the nearest point to the wire along the atomic path, the magnetic flux density is

$$B_w(0) = \frac{\mu_0 I}{2\pi z_a}, \tag{157}$$

which reaches 9.5×10^{-4} T at the maximum current of 0.5 A and z_a of 1.05×10^{-4} m. Therefore, the strongest $B_w(0)$ is 80 times ($= 9.5 \times 10^{-4}/0.119 \times 10^{-4}$) greater than B_n, 23 times ($= 9.5 \times 10^{-4}/0.42 \times 10^{-4}$) stronger than B_r, but 59 times ($= 558 \times 10^{-4}/9.5 \times 10^{-4}$) weaker than B_e. Also, $B_w(0)$ is ~300 times weaker than a typical main field [5, 37] (≥ 0.3 T) in Stern–Gerlach experiments (see Paragraph 2 in Discussion). Without including the induction exponent, CQD predicts the Frisch–Segrè experimental observation well already (Fig. 1 or Fig. 4). Consequently, the induction effect in the inner rotation chamber is initially neglected. However, it is included here for completeness and for the estimation of k_i. Below, zero time t is set to when an atom reaches the nearest point to the wire.

From Eq. 156, we estimate E_i by using the z component of the field along the path:

$$E_i = 4k_i|\gamma_e| \int_{-T_f/2}^{+T_f/2} \left|\frac{B_w(0)vt/z_a}{1+(vt/z_a)^2}\right| dt = 4k_i|\gamma_e|B_w(0)\frac{z_a}{v}\ln\left(\frac{T_f v}{2z_a}\right). \tag{158}$$

Substituting Eq. 157 gives

$$E_i = k_i \frac{2\mu_0|\gamma_e|}{\pi v}\ln\left(\frac{T_f v}{2z_a}\right) I. \tag{159}$$

Expressing in terms of the current, I, yields

$$W_{\text{cqd}} = \exp\left[-\sqrt{(c_{r0}/I)^2 + c_{rs}^2} - c_{r1}I^3 - c_{ri}I\right], \tag{160}$$

where

$$c_{r0} = 2\pi^2|\gamma_e|(B_r + B_n\cos\langle\theta_n\rangle)^2 z_a^2/(\mu_0 v), \tag{161}$$

$$c_{rs} = \pi|\gamma_e|B_n\sin\langle\theta_n\rangle\, z_a/v, \tag{162}$$

$$c_{r1} = \frac{\mu_0^3|\gamma_e|^2\gamma_n}{32\pi v^3}B_e(B_n\sin\langle\theta_n\rangle)^5/(B_r + B_n\cos\langle\theta_n\rangle)^6, \tag{163}$$

and

$$c_{ri} = k_i\frac{2\mu_0|\gamma_e|}{\pi v}\ln\left(\frac{T_f v}{2z_a}\right). \tag{164}$$

The four coefficients represent null-point rotation, rotation saturation, nuclear-resonant rotation, and induction rotation of the polar angle, respectively. While null-point rotation increases W_{cqd} with increasing current, nuclear-resonant rotation does the opposite.

If $k_i = 0$, Eq. 160 reduces to

$$W_4 = \exp\left[-\sqrt{(c_{r0}/I)^2 + c_{rs}^2} - c_{r1}I^3\right], \tag{165}$$

which is equivalent to Eq. 151. Further, if $c_{r1} = 0$, we reach

$$W_3 = \exp\left[-\sqrt{(c_{r0}/I)^2 + c_{rs}^2}\right], \tag{166}$$

which is another form of Eq. 152. Merging the above two equations, we obtain

$$W_4 = W_3 \exp(-c_{r1} I^3). \tag{167}$$

Finally, if $c_{rs} = 0$, we obtain

$$W_2 = \exp(- c_{r0}/I), \tag{168}$$

which is the same as Eq. 153.

Appendix 6. Uncertainty relation

If the initial co-quanta are isotropically distributed, CQD reproduces the quantum mechanical uncertainty relation.

First, we predict the expectation of the spin-angular-momentum projection, $\langle s_y \rangle$, along y, the direction of the atomic beam. The CQD prediction expression for the y axis is (Eq. 13)

$$|\hat{\mu}_e © \hat{\mu}_n\rangle_y = C_{+y}(\hat{\mu}_e, \hat{\mu}_n)|+y\rangle + C_{-y}(\hat{\mu}_e, \hat{\mu}_n) \exp(i\phi_{ey}) |-y\rangle, \tag{169}$$

where ϕ_{ey} denotes the azimuthal angle of $\vec{\mu}_e$ about y. Following Appendix 3 yields the wave function,

$$|\hat{\mu}_e\rangle_y = \cos\frac{\theta_{ey}}{2} |+y\rangle + \sin\frac{\theta_{ey}}{2} \exp(i\phi_{ey}) |-y\rangle, \tag{170}$$

where θ_{ey} denotes the polar angle of $\vec{\mu}_e$ relative to y. Note that $|+y\rangle$ here denotes "up" for magnetic moment and hence "down" for electron spin, and $|-y\rangle$ denotes the opposite state.

The expectation is

$$\langle s_y \rangle = -\frac{\hbar}{2}\cos^2\frac{\theta_{ey}}{2} + \frac{\hbar}{2}\sin^2\frac{\theta_{ey}}{2} = -\frac{\hbar}{2}\cos\theta_{ey}. \tag{171}$$

Second, we measure along z. The CQD prediction expression for the z axis is (Eq. 13)

$$|\hat{\mu}_e © \hat{\mu}_n\rangle_z = C_{+z}(\hat{\mu}_e, \hat{\mu}_n)|+z\rangle + C_{-z}(\hat{\mu}_e, \hat{\mu}_n) \exp(i\phi_{ez}) |-z\rangle. \tag{172}$$

We similarly derive the wave function (Appendix 3),

$$|\hat{\mu}_e\rangle_z = \cos\frac{\theta_{ez}}{2} |+z\rangle + \sin\frac{\theta_{ez}}{2} \exp(i\phi_{ez}) |-z\rangle, \tag{173}$$

where θ_{ez} and ϕ_{ez} denote the polar and azimuthal angles in relation to z.

We compute the standard deviation, Δs_z, as follows:

$$\langle s_z \rangle = -\frac{\hbar}{2}\cos^2\frac{\theta_{ez}}{2} + \frac{\hbar}{2}\sin^2\frac{\theta_{ez}}{2} = -\frac{\hbar}{2}\cos\theta_{ez}, \tag{174}$$

$$\langle s_z^2 \rangle = \left(-\frac{\hbar}{2}\right)^2 \cos^2\frac{\theta_{ez}}{2} + \left(\frac{\hbar}{2}\right)^2 \sin^2\frac{\theta_{ez}}{2} = \left(\frac{\hbar}{2}\right)^2, \tag{175}$$

and

$$\Delta s_z = \sqrt{\langle s_z^2 \rangle - \langle s_z \rangle^2} = \frac{\hbar}{2}\sin\theta_{ez}. \tag{176}$$

At this point, $\hat{\mu}_e$ has collapsed to $\pm z$; thus, the polar angle relative to x, $\theta_{ex} = \pi/2$. Now, the co-quantum distribution follows the heart shape (Eq. 24).

Third, we measure along x. The CQD prediction expression for the x axis is (Eq. 13)

$$|\hat{\mu}_e © \hat{\mu}_n\rangle_x = C_{+x}(\hat{\mu}_e, \hat{\mu}_n)|+x\rangle + C_{-x}(\hat{\mu}_e, \hat{\mu}_n) \exp(i\phi_{ex}) |-x\rangle. \tag{177}$$

Invoking $\theta_{ex} = \pi/2$, the heart shape (Eq. 24), and the identity $\cos\theta_{nz} = \sin\theta_{nx}\sin\phi_{nx}$, we follow Appendix 3 to similarly obtain for the $\pm z$ branch

$$\langle C_{+x}\rangle_n^2 = \int_{\pi/2}^{\pi}\int_0^{2\pi}\frac{1\mp\cos\theta_{nz}}{4\pi}\sin\theta_{nx}\,d\phi_{nx}d\theta_{nx} = \frac{1}{2} \tag{178}$$

and

$$\langle C_{-x}\rangle_n^2 = \int_0^{\pi/2}\int_0^{2\pi}\frac{1\mp\cos\theta_{nz}}{4\pi}\sin\theta_{nx}\,d\phi_{nx}d\theta_{nx} = \frac{1}{2}. \tag{179}$$

The even split between the two $\pm x$ branches is because the heart shape associated with either of the $\pm z$ branches is rotationally symmetric about the z axis. Thus, the wave function is

$$|\hat{\mu}_e\rangle_x = \frac{1}{\sqrt{2}}|+x\rangle + \frac{1}{\sqrt{2}}\exp(i\phi_{ex})\,|-x\rangle. \tag{180}$$

We derive the standard deviation, Δs_x, as follows:

$$\langle s_x\rangle = -\frac{\hbar}{2}\left(\frac{1}{\sqrt{2}}\right)^2 + \frac{\hbar}{2}\left(\frac{1}{\sqrt{2}}\right)^2 = 0, \tag{181}$$

$$\langle s_x^2\rangle = \left(-\frac{\hbar}{2}\right)^2\left(\frac{1}{\sqrt{2}}\right)^2 + \left(\frac{\hbar}{2}\right)^2\left(\frac{1}{\sqrt{2}}\right)^2 = \left(\frac{\hbar}{2}\right)^2, \tag{182}$$

and

$$\Delta s_x = \sqrt{\langle s_x^2\rangle - \langle s_x\rangle^2} = \frac{\hbar}{2}\,. \tag{183}$$

Fourth, combining Eq. 176 and 183 reaches

$$\Delta s_z \Delta s_x = \left(\frac{\hbar}{2}\sin\theta_{ez}\right)\cdot\frac{\hbar}{2}. \tag{184}$$

Substituting the identity, $\cos\theta_{ey} = \sin\theta_{ez}\sin\phi_{ez}$, into Eq. 171 yields

$$\frac{\hbar}{2}\left|\langle s_y\rangle\right| = \left[\left(\frac{\hbar}{2}\sin\theta_{ez}\right)\cdot\frac{\hbar}{2}\right]\cdot|\sin\phi_{ez}|. \tag{185}$$

Combining the above two equations yields

$$\Delta s_z \Delta s_x \cdot |\sin\phi_{ez}| = \frac{\hbar}{2}\left|\langle s_y\rangle\right|. \tag{186}$$

This uncertainty equality shows that the magnitude of the uncertainty product, $\Delta s_z \Delta s_x$, depends on not only $\langle s_y\rangle$ but also the initial phase, ϕ_{ez}, in relation to the first measurement axis. Therefore, the order of the z-x measurements matters.

Finally, invoking $|\sin\phi_{ez}| \leq 1$ reproduces exactly the familiar quantum mechanical uncertainty inequality for angular momenta,

$$\Delta s_z \Delta s_x \geq \frac{\hbar}{2}\left|\langle s_y\rangle\right|, \tag{187}$$

which takes on the equal sign when $\phi_{ez} = \pm\pi/2$.

Appendix 7. Entanglement

CQD in its current form construes anticorrelated entanglement as a pair of atoms having both opposing $\hat{\mu}_e$'s and $\hat{\mu}_n$'s (Fig. S6). The two atoms are delivered from the entanglement site to two Stern–Gerlach devices. Once the orientation of the external magnetic flux density $\vec{B}_0$ is chosen, the two $\hat{\mu}_e$'s are guaranteed to collapse to opposing states according to the branching condition because $\theta_{e1} + \theta_{e2} = \pi$ and $\theta_{n1} + \theta_{n2} = \pi$. For example, if atom 1 collapses to $+\hat{B}_0$ because $\theta_{n1} > \theta_{e1}$, atom 2 automatically collapses to $-\hat{B}_0$ because $\theta_{n2} < \theta_{e2}$ (as derived from $\pi - \theta_{n1} < \pi - \theta_{e1}$). Therefore, the co-quanta propagate with the principal quanta and determine the measurement outcomes.

The CQD prediction expressions for the two atoms are

$$|\hat{\mu}_e \copyright \hat{\mu}_n\rangle_1 = C_+(\hat{\mu}_e, \hat{\mu}_n)\left|+\hat{B}_0\right\rangle_1 + C_-(\hat{\mu}_e, \hat{\mu}_n)\exp(i\phi_{e1})\left|-\hat{B}_0\right\rangle_1 \tag{188}$$

and

$$|-\hat{\mu}_e \copyright -\hat{\mu}_n\rangle_2 = C_-(\hat{\mu}_e, \hat{\mu}_n)\left|+\hat{B}_0\right\rangle_2 + C_+(\hat{\mu}_e, \hat{\mu}_n)\exp(i\phi_{e2})\left|-\hat{B}_0\right\rangle_2. \tag{189}$$

The numeral subscripts denote the two atoms. The joint pre-collapse state function of the atom pair is written as $|\hat{\mu}_e \copyright \hat{\mu}_n\rangle_1 \otimes |-\hat{\mu}_e \copyright - \hat{\mu}_n\rangle_2$, where $\otimes$ denotes tensor product [59]. Because $C_+ \cdot C_- = 0$ and $C_\pm \cdot C_\pm = C_\pm$, the joint CQD prediction expression of the atom pair is given by

$$\begin{aligned} &|\hat{\mu}_e \copyright \hat{\mu}_n\rangle_1 \otimes |-\hat{\mu}_e \copyright -\hat{\mu}_n\rangle_2 \\ &= C_+\left|+\hat{B}_0\right\rangle_1 \otimes \left|-\hat{B}_0\right\rangle_2 + C_-\exp(i\Delta\phi)\left|-\hat{B}_0\right\rangle_1 \otimes \left|+\hat{B}_0\right\rangle_2, \end{aligned} \tag{190}$$

where $\Delta\phi = \phi_{e1} - \phi_{e2}$ and the common phase is removed.

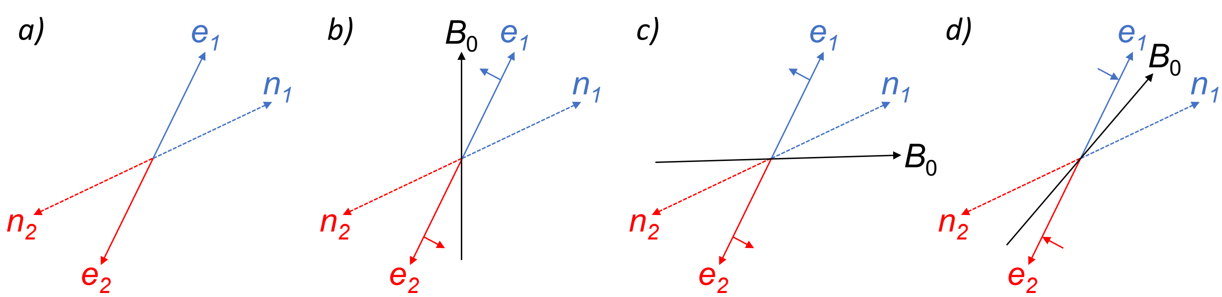

Fig. S6. Entanglement of the electron magnetic moments of two atoms. **(a)** At entanglement site. **(b) – (d)** At two Stern–Gerlach devices with three orientations of $\vec{B}_0$. *e*, electron magnetic moment; *n*, nuclear magnetic moment; subscripts 1 and 2, atoms 1 and 2. The short arrows indicate the directions of collapse determined by the branching condition, where the polar angles are relative to $\vec{B}_0$. In *d*, to facilitate comparison, one may mirror $\hat{\mu}_e$ about $\vec{B}_0$ because $\hat{\mu}_e$ precesses much faster than $\hat{\mu}_n$.

If $\Delta\phi$ is constant for a given experimental configuration, ensemble averaging Eq. 190, denoted by $\langle \quad \rangle_{n,e}$, yields the familiar quantum mechanical entangled wave function,

$$|\psi\rangle = \langle C_+\rangle_{n,e}\left|+\hat{B}_0\right\rangle_1 \otimes \left|-\hat{B}_0\right\rangle_2 + \langle C_-\rangle_{n,e}\exp(i\Delta\phi)\left|-\hat{B}_0\right\rangle_1 \otimes \left|+\hat{B}_0\right\rangle_2. \tag{191}$$

If both $\hat{\mu}_n$ and $\hat{\mu}_e$ of individual atoms are isotropically distributed, Appendix 3 provides $\langle C_\pm \rangle_{n,e} = 1/\sqrt{2}$, yielding

$$|\psi\rangle = \frac{1}{\sqrt{2}} \left|+\hat{B}_0\right\rangle_1 \otimes \left|-\hat{B}_0\right\rangle_2 + \frac{1}{\sqrt{2}} \exp(i\Delta\phi) \left|-\hat{B}_0\right\rangle_1 \otimes \left|+\hat{B}_0\right\rangle_2. \quad (192)$$

Here, the key to producing the above entangled wave function is the mutual exclusivity of the binary coefficients: $C_+ \cdot C_- = 0$. The pre-collapse "product state" in CQD, $|\hat{\mu}_e©\hat{\mu}_n\rangle_1 \otimes |-\hat{\mu}_e© - \hat{\mu}_n\rangle_2$, averages to an entangled wave function (i.e., not a product state). One can adapt the above derivation for correlated instead of anticorrelated entanglement.

A future direction is to explore CQD in relation to Bell's theorem [60]. An ideal experiment would follow the above derivation, where entangled pairs of alkali-metal atoms are delivered to two Stern–Gerlach devices with independent quantization axes. Shin *et al*. [61] published in 2019 an experiment in this direction. However, the quantization axes could not be controlled independently, and Bose-Einstein condensate helium-4 atoms in the long-lived metastable state $2^3\mathrm{S}_1$ instead of alkali-metal atoms were used. The same group also published in 2022 an experiment on the Bell inequality for motional degrees of freedom of massive particles, thus far reaching a maximum CHSH-Bell parameter of $S = 1.1$ [62].

Appendix 8. Two-stage Stern–Gerlach apparatus with a varying angle between the quantization axes

CQD can potentially be further verified with a two-stage Stern–Gerlach apparatus with a varying angle between the quantization axes. As usual, the first stage polarizes the atoms to the $+z$ state; however, the second stage is rotated by an arbitrary angle α about the y axis (the atomic beam axis). Below, the coordinates of the second stage are denoted with primes.

Using the heart-shaped angular distribution of the co-quanta (Eq. 24) and invoking both $\theta_{ez'} = \alpha$ and

$$\cos\theta_{nz} = \frac{1}{\sqrt{2}}(\cos\theta_{nz'} - \sin\theta_{nz'}\cos\phi_{nz'}), \tag{193}$$

CQD predicts the probability of collapsing to the $+z'$ state as

$$\langle C_{+z'}\rangle_n^2 = \int_\alpha^\pi \int_0^{2\pi} \frac{1-\cos\theta_{nz}}{4\pi} \sin\theta_{nz'}\, d\phi_{nz'} d\theta_{nz'} = \frac{(1+\cos\alpha)^2\,(2-\cos\alpha)}{4}. \tag{194}$$

In comparison, the standard literature [7, 30] predicts $\cos^2(\alpha/2)$ or $(1+\cos\alpha)/2$ (Eq. 16). At α of 0, $\pi/2$, and π, the typical angles in the literature, CQD and the literature predict the same probabilities of 1, $1/2$, and 0, respectively. In general, however, the ratio of the two predictions is

$$R_+ = [9 - (2\cos\alpha - 1)^2]/8, \tag{195}$$

which holds for $0 \le \alpha < \pi$ with π excluded to avoid $0/0$. The ratio peaks at α of $\pi/3$ with $R_+ = 9/8$ then decreases with increasing α. At $\alpha = 11\pi/12$, for example, $R_+ = 0.05$, with CQD predicting a much lower probability.

Peer-reviewed version of record

This manuscript except Appendices 7 – 8 and their referents is the version of the article submitted by the author to Journal of Physics B before copy editing. IOP Publishing Ltd is not responsible for any errors or omissions in this version of the manuscript, or any version derived from it. The Version of Record [63] is available online at https://doi.org/10.1088/1361-6455/acc149.